

Improving diffusion modeling in all-solid-state lithium batteries: a novel approach for grain boundary effects

Lena Scholz^{*a}, Yongliang Ou^{†b,c}, Blazej Grabowski^{‡b}, and Felix Fritzen^{§a}

^a*Institute of Applied Mechanics, University of Stuttgart, Universitätsstraße 32, 70569 Stuttgart, Germany*

^b*Institute for Materials Science, University of Stuttgart, Pfaffenwaldring 55, 70569 Stuttgart, Germany*

^c*Department of Materials Science and Engineering, Massachusetts Institute of Technology, 77 Massachusetts Ave, Cambridge, 02139, MA, USA*

April 15, 2025

Abstract

All-solid-state lithium-ion batteries offer promising advantages with respect to capacity, safety, and performance. The diffusion behavior of lithium ions in the contained polycrystalline solid-state electrolyte is crucial for battery function. While atomistic studies indicate that grain boundaries (GBs) and grain size significantly impact diffusivity, the corresponding effects are either neglected in simulations on larger scales or considered only under strong assumptions such as isotropy.

Our approach considers the fully resolved crystalline structure with a parametrization aligned with the atomistic perspective to describe diffusion along and across GBs. The approach is embedded into a finite element simulation using a novel collapsed interface element based on an analytical description in thickness direction. Results are governed by different and potentially anisotropic diffusion coefficients in bulk and GB domains. The mesoscale response is derived using linear computational homogenization to capture large-scale effects.

The novel collapsed interface description allows for a reconstruction of the 3D transport behavior within the GB domain without resolving it and is able to capture the relevant transport mechanisms such as channeling effects and concentration jumps. Grain size and GB volume fraction are expressed in terms of an affine parameter dependence and can be altered without any changes to geometry or mesh. Together with the observed dependence of the effective material response on the anisotropic GB parametrization, this leads to the identification of four distinct diffusion regimes, each with implications for the design of battery materials.

Keywords: grain boundary; ion diffusion; solid-state electrolyte; finite element method; interface transport

1 Introduction

Advancements in battery technology are crucial for decarbonizing both industry and daily life. *All-Solid-State Lithium-Ion Batteries* (ASSLIBs) represent an emerging alternative to conventional lithium-ion batteries [1]. In ASSLIBs the liquid electrolyte is replaced by a polycrystalline solid-state electrolyte. This does not only ensure operational safety [2] but also promises increased capacity and charging performance,

*scholz@mib.uni-stuttgart.de

†yongliang.ou@imw.uni-stuttgart.de

‡blazej.grabowski@imw.uni-stuttgart.de

§fritzen@mib.uni-stuttgart.de (corresponding author)

among other factors, and is, therefore, an object of ongoing research in academia and industrial application [3, 4].

The identification and design of optimized materials that are suitable for large-scale production is at the core of improving the performance of ASSLIBs [5–7]. Within the scope of this work we focus on lithium-based argyrodite-type materials for the solid-state electrolyte. Studies on the atomistic scale have reported that microstructural features beyond the crystal orientation, such as zero-dimensional (0D) defects (e.g., vacancies, dopant atoms), one-dimensional (1D) defects (e.g., dislocations), and two-dimensional (2D) defects (e.g., grain boundaries (GBs)) have a major impact on the local and overall material behavior [8,9]. The same holds in the case of variable chemical anion disorder, which was shown to result in drastic changes in ionic conductivity [10, 11]. Within the scope of this paper, attention is drawn to GB effects in particular.

With grain sizes down to or even smaller than $1.5\ \mu\text{m}$ [12], such materials contain a remarkable number of GBs. Many studies on the atomistic scale have observed grain size effects rooting from differing properties close to the GB domain [13–16]. However, the effect of GBs might be rather enhancing or limiting depending on the specific composition of the material under consideration [13]. Dawson et al. [17] noted an orthotropic diffusion behavior of the GBs. In view of reducing the massive computational demand for consideration of intricate atomic structures such as GBs, *ab initio*-based machine-learning interatomic potentials, e.g., moment tensor potential [18], have facilitated the consideration of larger systems over longer time spans and with higher accuracy [11]. Despite such notable progress, only isolated configurations can be studied. Hence, the effect of GBs on porosity, mechanical and electrical behavior, as well as ionic conductivity of materials, still remains an active field of research, e.g., Ref. [19]. This applies, in particular, to the remaining gap between the atomistic and application length and time scales of interest. In the following, we specifically focus on ionic conductivity, i.e., the diffusion of ions in polycrystalline solid materials.

Attempts to bridge this gap from an atomistic perspective often use simple analytical or empirical volume fraction-weighted averages of computed bulk and GB parameters to obtain effective properties for polycrystalline microstructures on mesoscale [15,17]. Note that most of these approaches trace back to very early insights from the last century [20,21] or derivations [22] which relate to the Wiener bounds [23] from permittivity or the bounds described by Voigt [24] and Reuss [25] in elasticity. However, realistic microstructural features of the polycrystalline geometry cannot be considered in these cases despite their relevance, especially for effective material properties [26].

Since the GB thickness is reported to be on the order of a few nanometers [11], a distinct separation of the GB width and the grain size (order of micrometers) persists. Therefore, a fully resolved consideration of the GB volume in continuum frameworks on the microscale is only feasible for simplified geometries that explore specific characteristics [27, 28]. In simulation frameworks for completely realistic ASSLIB setups, there is often no explicit account for the GB behavior, e.g., Ref. [29]. Besides the length separation between grains and GBs, the lack of reliable information on the actual, defect-specific material parameters (here: the tensorial diffusion coefficient) and their intrinsic stochasticity are reasons for the lack of consideration of GB-related diffusion in today’s models.

The efficient representation and modeling of interfaces and -phases arise in various mechanical application fields: These range from diffusion in membrane-like surface elements around impenetrable inclusions [30] to fracture and decohesion phenomena with discontinuities described by cohesive zone models; see, e.g., Refs. [31–33]. For the transport in coating layers in the context of ASSLIBs, dimensionally reduced models have been derived to avoid fully resolved layers and overcome simplified approximations [34]. Studies accounting for GB transport often follow the early Fisher model [35, 36] by only considering transport along the GB. Therefore, the concentration is assumed to be constant across the GB, while the in-plane transport is modeled by a single diffusion coefficient as well as a GB thickness parameter [37–39]. The GB itself is then represented by surface elements. Alternatively, cohesive elements can account for potential concentration jumps due to GB resistance [40]. The latter is the preferable choice, especially when it comes to more complex models accounting for fractures as well [41]. However, to our knowledge, there is still a lack of microscale finite element (FE) frameworks that account for anisotropic GB diffusion, meaning an explicit consideration of diffusion along and across the GBs as well as an account for the orientation of the GB. For the sake of completeness, we point out that diffusion in polycrystals has also been studied based on phase-field models with a varying extent of GB consideration [16, 42, 43]. An anisotropic parametrization of GBs was proposed within the context of phase-field models [44]. However, the need for classical FE descriptions remains.

With high-quality data describing the GB related diffusion emerging from dedicated low-scale simulations [11] on the horizon, we propose a FE framework that is informed by atomistic scale simulations. It explicitly accounts for anisotropic GB diffusion using a condensed GB representation. Through its use, we aim to facilitate an in-depth understanding of GB effects on larger scales. Furthermore, the collapsed interface representation enables parametric studies regarding the effect of the GB thickness or, equivalently, of the grain size.

The remainder of this article is structured as follows: In Section 2 the proposed diffusion model is introduced together with a suitable FE discretization: Starting from the Nernst-Planck equation the diffusion in the bulk is recapped (Section 2.1) before introducing a dimensionality reduced 'zero-thickness' ansatz for the GB diffusion in Section 2.2, followed by the FE discretization (Section 2.3) and the computational homogenization framework (Section 2.4). In order to reduce computation times at full accuracy, we exploit the affine structure of the problem in Section 2.5. In Section 3 a 2D validation example is introduced to prove consistency of the model assumptions. The captured effects on the diffusion behavior in 3D polycrystals are then discussed in detail in Section 4. In Section 5 the model is applied to a realistic setup using results from atomistic scale. Lastly, a conclusion and outlook are given in Section 6.

2 Constitutive model and discretization

2.1 Bulk diffusion

A model for the diffusion of a chemical species with concentration $c(\mathbf{x})$ is needed to simulate the motion of lithium ions. We describe the flux \mathbf{q} by the Nernst-Planck equation as considered in the context of ASSLIBs [45] via an advection term \mathbf{q}_v due to a velocity \mathbf{v} and the flux \mathbf{q}_f due to a driving force \mathbf{f} with

$$\mathbf{q} = \mathbf{q}_v + \mathbf{q}_f \quad \text{with } \mathbf{q}_v = c\mathbf{v}, \quad \mathbf{q}_f = \mathbf{D}_\Omega \mathbf{f}. \quad (1)$$

For solid-state electrolytes the velocity \mathbf{v} is zero, i.e., no advection needs to be considered, independently of the concentration c ($\mathbf{q}_v = \mathbf{0}$). The conductivity tensor $\mathbf{D}_\Omega \in \text{Sym}_+(\mathbb{R}^3)$ is symmetric and positive definite. It captures material symmetries (if any), i.e., given a symmetry group $\mathcal{G} \subseteq \text{SO}(3)$, the relation

$$\mathbf{D}_\Omega = \mathbf{G} \mathbf{D}_\Omega \mathbf{G}^\top, \quad \forall \mathbf{G} \in \mathcal{G}, \quad (2)$$

holds. If $\mathcal{G} \neq \text{SO}(3)$, then the actual conductivity tensor depends on the local crystal orientation \mathbf{Q} via

$$\mathbf{D}_\Omega = \mathbf{Q} \mathbf{D}_0 \mathbf{Q}^\top, \quad (3)$$

where \mathbf{D}_0 is the conductivity tensor in the reference coordinate system.

In the sequel, $\Omega \subset \mathbb{R}^3$ is a representative volume element of the material as shown in Figure 1, and the coordinate $\mathbf{x} \in \Omega$ is used to emphasize potential spatial dependencies. Time dependencies are not stated explicitly in favor of a simplified notation. The driving force \mathbf{f} in eq. (1) is composed of two additive contributions:

$$\mathbf{f}(\mathbf{x}) = \mathbf{f}_c(\mathbf{x}) + \mathbf{f}_E(\mathbf{x}) \quad \text{with } \mathbf{f}_c(\mathbf{x}) = -\nabla c(\mathbf{x}), \quad \mathbf{f}_E(\mathbf{x}) = \frac{ze}{k_B T} c(\mathbf{x}) \mathbf{E}(\mathbf{x}). \quad (4)$$

The first part $\mathbf{f}_c(\mathbf{x})$ contains the driving force due to the gradient of the chemical concentration $c(\mathbf{x})$ according to Fick's first law. The second part $\mathbf{f}_E(\mathbf{x})$ accounts for electromigration due to the presence of an electric field $\mathbf{E}(\mathbf{x})$. Here z denotes the valence of the ionic species, e is the elementary charge, k_B denotes the Boltzmann constant, and T the absolute temperature. Although particularly $\mathbf{f}_E(\mathbf{x})$ is of interest, we confine attention to the driving forces \mathbf{f}_c according to Fick's law in order to determine the effective diffusivity. The investigation of contributions due to \mathbf{f}_E is postponed to a later stage.

Within the solid electrolyte (that is, away from the active material and the anode/cathode), ions are neither produced nor annihilated. In this region, the ion concentration during charging or discharging settles at a steady state, fulfilling the balance equation

$$\mathbf{q}(\mathbf{x}) \cdot \nabla = 0 \quad \text{in } \Omega, \quad + \text{ boundary conditions (BC)}. \quad (5)$$

Note also that, due to the small size of Ω , the variations of the absolute value of the concentration $c(\mathbf{x})$ are small, matching results of, e.g., Ref. [11] on the atomistic scale of the material. At the same time, the gradient $\nabla c(\mathbf{x})$ can take substantial values, and relevant driving forces can emerge from these small fluctuations.

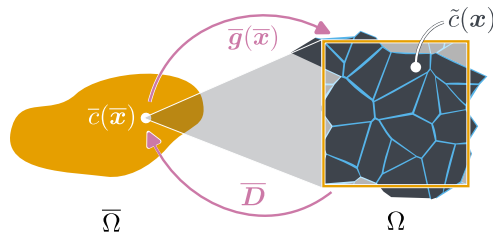


Figure 1: Relation between macroscopic position $\bar{\mathbf{x}} \in \bar{\Omega}$ (mesoscale) and corresponding periodic microscopic polycrystalline sample Ω (microscale) in the context of linear computational homogenization. The quantities introduced in eq. (6), as well as the macroscopic diffusion tensor $\bar{\mathbf{D}}$, are indicated for reference.

Regarding the BCs, we limit attention to periodic fluctuation conditions for the concentration $c(\mathbf{x})$. This choice is motivated by established results for linear computational homogenization [46] and follows the schematic in Figure 1:

$$c(\mathbf{x}) = \bar{c}(\bar{\mathbf{x}}) + \bar{\mathbf{g}}(\bar{\mathbf{x}}) \cdot \mathbf{x} + \tilde{c}(\mathbf{x}). \quad (6)$$

It is composed of the macroscopic concentration $\bar{c}(\bar{\mathbf{x}})$ at the macroscopic position $\bar{\mathbf{x}} \in \bar{\Omega} \subset \mathbb{R}^3$, a contribution of the imposed macroscopic concentration gradient $\bar{\mathbf{g}}$, and the periodic concentration fluctuation field $\tilde{c}(\mathbf{x})$. Note that $\bar{\mathbf{g}}$ could be replaced by an equivalent effective driving force, e.g., due to an applied electric field $\bar{\mathbf{E}}$ (cf. Remark 2).

Solving eq. (5) with the unit gradients $\bar{\mathbf{g}}_k = \mathbf{e}_k$ ($k = 1, 2, 3$) applied as boundary conditions yields three linear problems. The macroscopic diffusion tensor $\bar{\mathbf{D}}$ follows from the corresponding averaged gradient and flux fields, see Section 2.4.2.

Remark 1. *The presented steady-state diffusion problem is equivalent to a steady-state heat conduction problem or to electrostatics. Therefore, established discretizations, e.g., using finite elements, can readily be applied to the elliptic problem.*

Remark 2. *The macroscopic gradient $\bar{\mathbf{g}}$ introduces a spatially constant driving force $\mathbf{f}_{c,0} = -\bar{\mathbf{g}}$. This is equivalent to an external electric field (assumed constant inside of the microstructure) $\bar{\mathbf{E}} = -\frac{k_{\text{B}}T}{ze} \frac{1}{\bar{c}} \bar{\mathbf{g}}$. Therefore, the model presented herein also calculates the sought-after diffusion tensor $\bar{\mathbf{D}}$ in the presence of electric fields.*

2.2 Interface diffusion with in-surface diffusion

2.2.1 Assumptions and definitions

In our recent study [11], the diffusion parameters of both the bulk and different GBs of the argyrodite $\text{Li}_6\text{PS}_5\text{Cl}$ have been assessed through molecular dynamics simulations using tuned machine-learning interatomic potentials. It was found that (i) the diffusivity of the GB varied considerably from that of the bulk, and (ii) the diffusion coefficients along and across the GB are different. Further, the dependency on the temperature T introduced via the Arrhenius relation [47]

$$D(T) = D_0 \exp\left(-\frac{E_{\text{a}}}{k_{\text{B}}T}\right) \quad (7)$$

potentially differs due to the phase-specific fitted constant D_0 and activation energy E_{a} . The Boltzmann constant is denoted with k_{B} here.

To model this behavior, we propose a special-purpose FE type inspired by cohesive zone elements used in mechanical problems (see Ref. [33] for a comprehensive review). The model is put into the context of GBs [48–50] to deal with the aforementioned aspects. In a mechanical setting, cohesive elements allow

for a displacement jump $\boldsymbol{\delta}$ across the interface, defining the traction vector $\mathbf{t}(\boldsymbol{\delta})$ (e.g., Refs. [51–53]). We adopt the concept of a discontinuity between adjacent bulk domains for the concentration $c(\mathbf{x})$ by connecting them with a continuous function through a virtual finite-thickness interface.

We systematically construct the interfacial model and the related special-purpose element building on the following assumptions:

[A1] The variable to be modeled is the concentration $c(\mathbf{x})$. It is assumed to be continuous in the bulk as well as within and throughout the interface, i.e., the GBs.

[A2] The surrounding mesh, representing a polycrystal based on the Voronoi tessellation [54–56], is assumed to be tetrahedral.

[A3] The interface width $2h$ is much smaller than the grain size L_{grain} . Therefore, the interface element is collapsed along the out-of-plane direction \mathbf{n} . In the FE mesh, the elements will appear to have zero thickness, which aligns with the assumed separation of length scales. The (usually small) GB volume $v_{\text{GB}} = 2hA$ added to the representative volume element will partially be corrected during post-processing of the results (see Section 2.4.1). The vector of a point within the interface is decomposed based on the interface normal \mathbf{n} (see also Figure 2a) according to:

$$\mathbf{x} = \mathbf{x}_{\parallel} + \mathbf{x}_{\perp}, \quad \mathbf{x}_{\parallel} = (\mathbf{I} - \mathbf{n} \otimes \mathbf{n}) \mathbf{x} = x_{\parallel} \mathbf{e}_t, \quad \mathbf{x}_{\perp} = (\mathbf{n} \cdot \mathbf{x}) \mathbf{n} = x_{\perp} \mathbf{n}. \quad (8)$$

Here, \mathbf{e}_t denotes an unit vector in the interface plane. The same decomposition applies to vector-valued quantities such as the flux \mathbf{q} (see Section 2.2.2).

[A4] Within the GB region, a transversely isotropic diffusion tensor $\mathbf{D}_{\text{GB},0} \in \text{Sym}_+$ is assumed. The GB-attached local coordinate system is defined as $\{\mathbf{e}_{t1}, \mathbf{e}_{t2}, \mathbf{n}\}$, i.e., the two orthonormal tangential basis vectors followed by the normal orientation of the GB, with coordinates $\underline{\zeta} = [\zeta_{t1}, \zeta_{t2}, \zeta_n]$ (see also Figures 2b and 2c). With this simplification, the matrix representation of the diffusion tensor reduces to

$$\mathbf{D}_{\text{GB},0} = \begin{bmatrix} D_{\parallel} & 0 & 0 \\ 0 & D_{\parallel} & 0 \\ 0 & 0 & D_{\perp} \end{bmatrix}_{(t1,t2,n)}, \quad (9)$$

where D_{\parallel} and D_{\perp} are the in-plane and through-plane diffusion coefficients, respectively.

[A5] In the local coordinate system we assert a quadratic ansatz in the through-thickness direction for each $\underline{\zeta}_t = [\zeta_{t1}, \zeta_{t2}]$, i.e.,

$$c(\zeta_{t1}, \zeta_{t2}, \zeta_n) = \sum_{j=0}^2 \alpha_j(\underline{\zeta}_t) \left(\frac{\zeta_n}{h} \right)^j, \quad (10)$$

which is motivated by the following model problem: When investigating a two-dimensional planar channel-like problem in the system $\{\mathbf{e}_{t1}, \mathbf{e}_n\}$ with ion in-/outflux $s_{+1}(\zeta_{t1})$ on top and $s_{-1}(\zeta_{t1})$ on bottom (cf. Figure 2b) the in-plane flux must depend on ζ_{t1} . By combining the analytical expression for the flux at top and bottom one finds:

$$\left. \begin{aligned} q(\zeta_n = h) &= -D_{\perp} \left(\frac{\alpha_1(\zeta_{t1})}{h} + \frac{2\alpha_2(\zeta_{t1})}{h} \right) \stackrel{!}{=} s_{+1}(\zeta_{t1}) \\ -q(\zeta_n = -h) &= -D_{\perp} \left(\frac{\alpha_1(\zeta_{t1})}{h} - \frac{2\alpha_2(\zeta_{t1})}{h} \right) \stackrel{!}{=} -s_{-1}(\zeta_{t1}) \end{aligned} \right\} \alpha_2(\zeta_{t1}) = \frac{h}{4D_{\perp}} (s_{+1}(\zeta_{t1}) + s_{-1}(\zeta_{t1})). \quad (11)$$

This implies that quadratic modes enable a net flux into and out of the GB, which is infeasible when considering only linear concentration profiles in the thickness direction. Furthermore, this mechanism enables ion channeling along the GBs.

[A6] Mechanical separation of the interface is not considered.

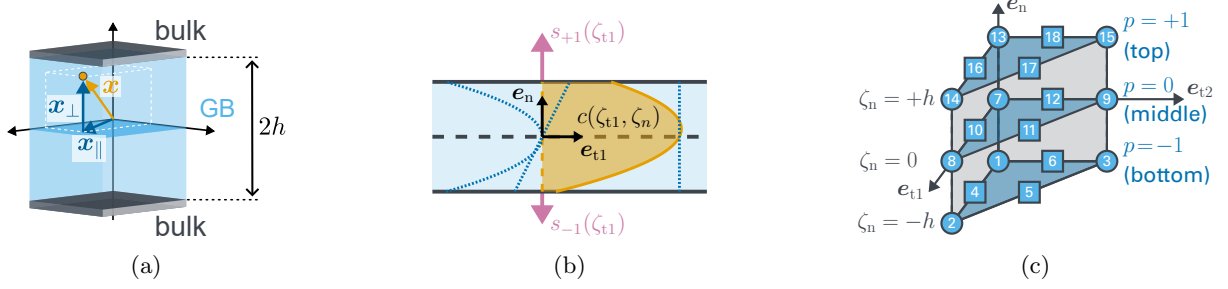


Figure 2: **(a)**: Interface of thickness $2h$ and the split into tangential and normal coordinates. **(b)**: Ion flux in a 2D channel example with in-/outflux on top and bottom. The concentration profile $c(\zeta_{t1}, \zeta_n)$ as well as the required constant, linear and quadratic modes (dotted lines) are given. **(c)**: Exploded view of the ζ_n -collapsed quadratic prism element: Nodes 1-6 constitute the *bottom* ($p = -1$), nodes 7-12 the *middle* ($p = 0$), and nodes 13-18 the *top* layer ($p = 1$).

2.2.2 Model properties

The diffusion constants $D_{\parallel}, D_{\perp} > 0$ characterize the behavior of the GB alongside the GB half-width h . Regarding the amplitude of the ion flux parallel q_{\parallel} and perpendicular q_{\perp} to the interface, we obtain the relation

$$q_{\perp} = \mathbf{q} \cdot \mathbf{n} = -D_{\perp} \frac{\partial c(\zeta)}{\partial \zeta_n} \sim \frac{D_{\perp}}{h} \llbracket c \rrbracket, \quad (12)$$

$$q_{\parallel} = |(\mathbf{I} - \mathbf{n} \otimes \mathbf{n}) \mathbf{q}| = D_{\parallel} \sqrt{|c \otimes \nabla|^2 - \left(\frac{\partial c(\zeta)}{\partial \zeta_n} \right)^2} \sim D_{\parallel} |\nabla_{\parallel} c|, \quad (13)$$

by means of the decomposition in eq. (8), where $\llbracket c \rrbracket$ denotes the concentration jump across the GB and $\nabla_{\parallel}[\cdot] := (\mathbf{I} - \mathbf{n} \otimes \mathbf{n}) \nabla[\cdot]$ is the tangential gradient. In particular, q_{\parallel} does not explicitly depend on h , while q_{\perp} does. In the limit case where $h \rightarrow 0$ or $D_{\perp} \rightarrow \infty$ (or both), the diffusion q_{\perp} in the through-thickness direction also tends to infinity, which recovers the case of a classical bulk-only simulation, i.e., it renders the proposed GB model obsolete. Inversely, this observation nicely illustrates implicit assumptions of such "classical" simulations, i.e., assumed zero ion flow resistance of the GBs.

In the case where $D_{\Omega} = D_{\perp} = D_{\parallel}$, the GB should not influence the response at all. This case will be used to motivate the volume fraction compensation strategy for the computation of effective properties in Section 2.4.2.

2.3 Finite element implementation

2.3.1 Bulk

As for the bulk material, we use isoparametric, quadratic tetrahedra (e.g., TET10 in Abaqus) with the vector of shape functions $\underline{N}_{\Omega}(\boldsymbol{\eta}) \in \mathbb{R}^{1 \times 10}$ for the reference coordinates $\boldsymbol{\eta} = [\eta_1, \eta_2, \eta_3]$ (see Appendix A.1). Using isoparametric finite elements results in the gradient operator \underline{B}_{Ω} to depend on the gradient operator $\underline{B}_{\Omega}^{\text{ref}} \in \mathbb{R}^{3 \times 10}$ in the reference element Ω_{ref}^e and on the Jacobian

$$\underline{J}_{\Omega}^{(i)}(\boldsymbol{\eta}) = \underline{B}_{\Omega}^{\text{ref}}(\boldsymbol{\eta}) \underline{X}_{\Omega}^{(i)}, \quad (14)$$

where $\underline{X}_{\Omega}^{(i)} \in \mathbb{R}^{10 \times 3}$ is a matrix containing the coordinates of the 10 nodes of the i -th bulk element. The gradient operator then reads $\underline{B}_{\Omega}(\boldsymbol{\eta}) = \underline{J}_{\Omega}^{-1}(\boldsymbol{\eta}) \underline{B}_{\Omega}^{\text{ref}}(\boldsymbol{\eta})$ where the superscript i is omitted for readability. As per the deployed cubature scheme, we have resorted to $n_{\text{GP}}^{\text{T10}} = 4$ integration points $\boldsymbol{\eta}_j$ with corresponding integration weights $\omega_j = v^e/4$ ($j = 1, \dots, 4 = n_{\text{GP}}^{\text{T10}}$) given the element volume v^e .

In the following, an isotropic bulk material $\underline{D}_{\Omega} \equiv \mathbf{D}_{\Omega} = D_{\Omega} \mathbf{I}$ is assumed¹. This assumption is valid for materials exhibiting isotropic or cubic symmetry, with the latter being the case for promising argyrodite

¹The coefficient matrix \underline{D}_{Ω} is equivalent to the tensor \mathbf{D}_{Ω} , but in a fixed coordinate system. Only then the algebraic operations for assembly of the FE system can be expressed in a sleek notation.

materials [57] such as $\text{Li}_6\text{PS}_5\text{Cl}$ that was also studied in joint work with material scientists [11]. The resulting element stiffness matrix $\underline{\underline{K}}_\Omega^e$ in the bulk then reads

$$\underline{\underline{K}}_\Omega^e = \sum_{j=1}^{n_{\text{GP}}^\Omega} \omega_j \underline{\underline{B}}_\Omega^\top(\eta_j) \underline{\underline{D}}_\Omega \underline{\underline{B}}_\Omega(\eta_j) = D_\Omega \sum_{j=1}^{n_{\text{GP}}^\Omega} \omega_j \underline{\underline{B}}_\Omega^\top(\eta_j) \underline{\underline{B}}_\Omega(\eta_j). \quad (15)$$

2.3.2 Special purpose surface diffusion element

Building on the considerations of Section 2.2, we suggest a shape function based on the following tensor-product ansatz: On each of the three planes ($p \in \{-1, 0, 1\}$) in Figure 2c, we introduce classical two-dimensional quadratic shape functions $\underline{N}_{\text{P2}}(\zeta_{t1}, \zeta_{t2}) \in \mathbb{R}^{1 \times 6}$ through a six node triangular element (see Appendix A.2) with integration weights ν_i . In conjunction with the used quadratic tetrahedral elements in the bulk, this enforces the assumed continuity of $c(\mathbf{x})$ in Assumption [A1]. Then, on each of the three ζ_n levels, a planar interpolation is pursued, leading to a total of $3 \times 6 = 18$ nodes per element. The element degree of freedom vector \underline{c}^e is partitioned along the three layers according to:

$$\underline{c}^e = \begin{bmatrix} \underline{c}_{-1}^e \\ \underline{c}_0^e \\ \underline{c}_1^e \end{bmatrix} \in \mathbb{R}^{18}. \quad (16)$$

The surface interpolated data on the three layers

$$c_p^e(\zeta_{t1}, \zeta_{t2}) = \underline{N}_{\text{P2}}(\zeta_{t1}, \zeta_{t2}) \underline{c}_p^e, \quad p \in \{-1, 0, 1\}, \quad (17)$$

is further interpolated at the through-thickness coordinate $\zeta_n \in [-h, h]$ by a quadratic Lagrange basis $\{\mathcal{L}_{-1}, \mathcal{L}_0, \mathcal{L}_1\}$, i.e.,

$$\mathcal{L}_p(\zeta_n) = \prod_{\beta \in \{-1, 0, 1\} \setminus \{p\}} \frac{\zeta_n - \beta h}{(p - \beta)h}, \quad p \in \{-1, 0, 1\}. \quad (18)$$

Putting the staggered interpolation together, the shape function within the prismatic GB element $\underline{N}_{\text{GB}}$ gets

$$c^e(\zeta_{t1}, \zeta_{t2}, \zeta_n) = \sum_{p=-1}^1 \mathcal{L}_p(\zeta_n) c_p^e(\zeta_{t1}, \zeta_{t2}) = \sum_{p=-1}^1 \mathcal{L}_p(\zeta_n) \underline{N}_{\text{P2}}(\zeta_{t1}, \zeta_{t2}) \underline{c}_p^e = \underline{N}_{\text{GB}}(\zeta_{t1}, \zeta_{t2}, \zeta_n) \underline{c}^e, \quad (19)$$

i.e., $\underline{N}_{\text{GB}} = [\mathcal{L}_{-1}(\zeta_n) \underline{N}_{\text{P2}}(\underline{\zeta}_t) \quad \mathcal{L}_0(\zeta_n) \underline{N}_{\text{P2}}(\underline{\zeta}_t) \quad \mathcal{L}_{+1}(\zeta_n) \underline{N}_{\text{P2}}(\underline{\zeta}_t)] \in \mathbb{R}^{1 \times 18}$. The gradient of the concentration within the GB results from applying the product rule

$$\begin{aligned} \nabla c^e(\zeta_{t1}, \zeta_{t2}, \zeta_n) &= \begin{bmatrix} \frac{\partial \underline{N}_{\text{GB}}}{\partial \zeta_{t1}} \\ \frac{\partial \underline{N}_{\text{GB}}}{\partial \zeta_{t2}} \\ \frac{\partial \underline{N}_{\text{GB}}}{\partial \zeta_n} \end{bmatrix} \underline{c}^e = \sum_{p=-1}^1 \left(\begin{bmatrix} 1 & 0 \\ 0 & 1 \\ 0 & 0 \end{bmatrix} \underline{B}_{\text{P2}}^{\text{ref}}(\underline{\zeta}_t) \mathcal{L}_p(\zeta_n) + \begin{bmatrix} 0 \\ 0 \\ 1 \end{bmatrix} \frac{\partial \mathcal{L}_p(\zeta_n)}{\partial \zeta_n} \underline{N}_{\text{P2}}(\underline{\zeta}_t) \right) \underline{c}_p^e \quad (20) \\ &= \begin{bmatrix} 1 & 0 \\ 0 & 1 \\ 0 & 0 \end{bmatrix} \underline{B}_{\text{GB},\parallel}^{\text{ref}}(\underline{\zeta}_t, \zeta_n) \underline{c}^e + \begin{bmatrix} 0 \\ 0 \\ 1 \end{bmatrix} \underline{B}_{\text{GB},\perp}^{\text{ref}}(\underline{\zeta}_t, \zeta_n) \underline{c}^e = \underline{B}_{\text{GB}}^{\text{ref}}(\zeta_{t1}, \zeta_{t2}, \zeta_n) \underline{c}^e, \quad (21) \end{aligned}$$

matching the GB coordinate system in Figure 2.

In the following, the element-specific gradient operators $\underline{B}_{\text{GB},\parallel}^{\text{ref}}$ and $\underline{B}_{\text{GB},\perp}^{\text{ref}}$ are derived. The operator $\underline{B}_{\text{GB},\parallel}^{\text{ref}} \in \mathbb{R}^{2 \times 18}$ defined in the two-dimensional reference system $\{e_{t1}, e_{t2}\}$ needs to be related to the 3D coordinate system of the element. The nodal positions of the element $\underline{X}_{\text{GB}}^{(i)} \in \mathbb{R}^{6 \times 3}$ in the global coordinate system are identical on all three layers due to the zero-thickness of the element. We construct a transformation matrix $\underline{W} \in \mathbb{R}^{3 \times 2}$, which consists of two vectors that form a 2D orthonormal basis containing the interface element. The 2D representation of the nodal positions in this system is then given by

$$\underline{\tilde{X}}_{\text{GB}} = \underline{X}_{\text{GB}} \underline{W} \in \mathbb{R}^{6 \times 2}. \quad (22)$$

By means of the in-plane gradient operator $\underline{B}_{P2}^{\text{ref}} \in \mathbb{R}^{2 \times 6}$ the inverse of the Jacobian \underline{J}_{GB} yields the gradient operator which is then projected back to the global 3D system, i.e.,

$$\underline{B}_{GB,\parallel}(\zeta_t, \zeta_n) = \underline{W} \underline{J}_{GB}^{-1} \underline{B}_{GB,\parallel}^{\text{ref}} \in \mathbb{R}^{3 \times 18} \quad \text{with } \underline{J}_{GB} = \underline{B}_{P2}^{\text{ref}} \underline{\tilde{X}}_{GB} \in \mathbb{R}^{2 \times 2}. \quad (23)$$

Note the dependence on ζ_n due to the implicit representation of the normal direction. The contribution in the normal direction is directly given by multiplication with the interface normal:

$$\underline{B}_{GB,\perp}(\zeta_t, \zeta_n) = \underline{n} \underline{B}_{GB,\perp}^{\text{ref}}. \quad (24)$$

For the assembly of the element stiffness matrices, the orthogonality of normal and in-plane contributions is exploited:

$$\underline{K}_{GB}^e = \sum_{j=1}^{n_{GP}^{C18}} \nu_j \int_{-h}^h D_{\parallel} \underline{B}_{GB,\parallel}^T(\zeta_{t(j)}, \zeta_n) \underline{B}_{GB,\parallel}(\zeta_{t(j)}, \zeta_n) + D_{\perp} \underline{B}_{GB,\perp}^T(\zeta_{t(j)}, \zeta_n) \underline{B}_{GB,\perp}(\zeta_{t(j)}, \zeta_n) d\zeta_n. \quad (25)$$

The integration over the interface plane is performed by means of the respective cubature scheme with integration weights ν_i ($i = 1, \dots, 7 = n_{GP}^{C18}$) and in-plane integration points $\zeta_{t(j)}$. Due to the tensor product ansatz, the integration over the thickness of the element can be performed analytically, yielding constant prefactors independent of the specific element shape in the plane. The element stiffness matrix can be decomposed in an in-plane contribution $\underline{K}_{\parallel}^e$ and a normal contribution \underline{K}_{\perp}^e :

$$\underline{K}_{\parallel}^e = \frac{D_{\parallel} h}{15} \begin{bmatrix} 4[*] & 2[*] & -1[*] \\ 2[*] & 16[*] & 2[*] \\ -1[*] & 2[*] & 4[*] \end{bmatrix} \in \mathbb{R}^{18 \times 18} \quad \text{with } [*] = \sum_{j=1}^{n_{GP}^{C18}} \nu_j \underline{B}_{P2}^T(\zeta_{t(j)}) \underline{B}_{P2}(\zeta_{t(j)}) \in \mathbb{R}^{6 \times 6}, \quad (26)$$

$$\underline{K}_{\perp}^e = \frac{D_{\perp}}{6h} \begin{bmatrix} 7[**] & -8[**] & 1[**] \\ -8[**] & 16[**] & -8[**] \\ 1[**] & -8[**] & 7[**] \end{bmatrix} \in \mathbb{R}^{18 \times 18} \quad \text{with } **[**] = \sum_{j=1}^{n_{GP}^{C18}} \nu_j \underline{N}_{P2}^T(\zeta_{t(j)}) \underline{N}_{P2}(\zeta_{t(j)}) \in \mathbb{R}^{6 \times 6}. \quad (27)$$

Note that the element stiffness matrices consist of nine identical blocks with different prefactors, which form a symmetric pattern. This allows for an efficient assembly of the matrices under consideration of the material- and microstructure-specific parameters D_{\parallel} , D_{\perp} , h .

Remark 3. The notation for the block-symmetric structure of the stiffness matrices $\underline{K}_{\parallel}^e$ and \underline{K}_{\perp}^e could be condensed by means of the Kronecker product, i.e.,

$$\underline{K}_{\parallel}^e = \frac{D_{\parallel} h}{15} \begin{bmatrix} 4 & 2 & -1 \\ 2 & 16 & 2 \\ -1 & 2 & 4 \end{bmatrix} \otimes [*], \quad \underline{K}_{\perp}^e = \frac{D_{\perp}}{6h} \begin{bmatrix} 7 & -8 & 1 \\ -8 & 16 & -8 \\ 1 & -8 & 7 \end{bmatrix} \otimes **[**]. \quad (28)$$

However, we stick to the given notation in order to avoid ambiguity with respect to the outer product, commonly denoted with \otimes as well.

Remark 4. In general, the material parameters of a GB depend on the orientation of its interface and the neighboring grains. The structure of the global FE system allows for such a direct interface-specific parametrization without any overhead. For simplicity, however, we assume identical GB properties for all interfaces in the geometry for now. This will allow for an in-depth analysis of the transport mechanisms in Section 4.

2.3.3 Periodicity constraints and overall system

Following the homogenization setting in eq. (6), the imposed macroscopic driving force \bar{g} enters the FE system via the right-hand side. The assembled global system to be solved comprises contributions from the volume elements representing the bulk $[\cdot]_{\Omega}$ as well as the in-plane $[\cdot]_{\parallel}$ and normal $[\cdot]_{\perp}$ contributions from the suggested interface elements. The resulting linear system to be solved for the degrees of freedom (DOFs) of the fluctuation field \tilde{c} reads

$$\left(\underline{K}_{\Omega} + \underline{K}_{\parallel} + \underline{K}_{\perp} \right) \tilde{c} = r_{\Omega} + r_{\parallel} + r_{\perp} \quad (29)$$

with the respective contributions

$$\underline{\underline{K}}_{[\cdot]} = \sum_{i=1}^{n_{\text{el}}^{[\cdot]}} \left(\underline{\underline{L}}_{[\cdot]}^{(i)} \right)^{\top} \underline{\underline{K}}_{[\cdot]}^{(i)} \underline{\underline{L}}_{[\cdot]}^{(i)}, \quad \underline{\underline{r}}_{[\cdot]} = - \sum_{i=1}^{n_{\text{el}}^{[\cdot]}} \left(\underline{\underline{L}}_{[\cdot]}^{(i)} \right)^{\top} \underline{\underline{K}}_{[\cdot]}^{(i)} \underline{\underline{X}}_{[\cdot]}^{(i)} \underline{\underline{g}}. \quad (30)$$

for given scatter matrices $\underline{\underline{L}}_{[\cdot]}^{(i)}$ referring to the individual elements. The positions of the nodes within an element are denoted by $\underline{\underline{X}}_{\Omega}^{(i)} \in \mathbb{R}^{10 \times 3}$ for the bulk and $\underline{\underline{X}}_{\text{GB}}^{(i)} \in \mathbb{R}^{18 \times 3}$ for the GB domain. To enforce periodicity between primary and replica DOFs $\tilde{\underline{\underline{c}}}_{\text{p}}$ and $\tilde{\underline{\underline{c}}}_{\text{r}}$ on the boundary we introduce two projectors $\underline{\underline{P}}_{\text{per}} \in \mathbb{R}^{d \times d}$ and $\underline{\underline{P}}_{\text{f}} \in \mathbb{R}^{d \times d_{\text{f}}}$: The d_{f} free DOFs in $\tilde{\underline{\underline{c}}}_{\text{f}}$ are first scattered to the full system size d by using $\underline{\underline{P}}_{\text{f}}$. With $\underline{\underline{P}}_{\text{per}}$ the entire set of DOFs is then obtained by keeping the free DOFs and reconstructing the constrained DOFs $\tilde{\underline{\underline{c}}}_{\text{r}}$ on the boundary from $\tilde{\underline{\underline{c}}}_{\text{f}}$. This can be expressed in the following symbolic notation:

$$\tilde{\underline{\underline{c}}} = \begin{bmatrix} \tilde{\underline{\underline{c}}}_{\text{p}} \\ \tilde{\underline{\underline{c}}}_{\text{r}} \\ \tilde{\underline{\underline{c}}}_{\text{i}} \end{bmatrix} = \begin{bmatrix} 1 & 0 & 0 \\ * & 0 & 0 \\ 0 & 0 & 1 \end{bmatrix} \begin{bmatrix} 1 & 0 \\ 0 & 0 \\ 0 & 1 \end{bmatrix} \begin{bmatrix} \tilde{\underline{\underline{c}}}_{\text{p}} \\ \tilde{\underline{\underline{c}}}_{\text{f}} \end{bmatrix} =: \underline{\underline{P}}_{\text{per}} \underline{\underline{P}}_{\text{f}} \tilde{\underline{\underline{c}}}_{\text{f}}, \quad (31)$$

where $*$ encodes the periodicity constraints and $\tilde{\underline{\underline{c}}}_{\text{i}}$ denotes the non-boundary DOFs inside the domain. Hence, one needs to solve the following system

$$\underline{\underline{P}}_{\text{f}}^{\top} \underline{\underline{P}}_{\text{per}}^{\top} \left(\underline{\underline{K}}_{\Omega} + \underline{\underline{K}}_{\parallel} + \underline{\underline{K}}_{\perp} \right) \underline{\underline{P}}_{\text{per}} \underline{\underline{P}}_{\text{f}} \tilde{\underline{\underline{c}}}_{\text{f}} = \underline{\underline{P}}_{\text{f}}^{\top} \underline{\underline{P}}_{\text{per}}^{\top} \left(\underline{\underline{r}}_{\Omega} + \underline{\underline{r}}_{\parallel} + \underline{\underline{r}}_{\perp} \right) \quad (32)$$

for the vector of free DOFs $\tilde{\underline{\underline{c}}}_{\text{f}} = \underline{\underline{P}}_{\text{f}}^{\top} \tilde{\underline{\underline{c}}} \in \mathbb{R}^{d_{\text{f}}}$ that is reduced in size. The full solution vector of the fluctuation field $\tilde{\underline{\underline{c}}}$ is then recovered by reapplying $\underline{\underline{P}}_{\text{f}}$ and $\underline{\underline{P}}_{\text{per}}$ again as given in eq. (31).

2.4 Homogenization framework: effective properties and analytical bounds

2.4.1 Geometry-specific characteristic quantities

Following Assumption [A2], the considered spatial domain is given as a Voronoi tessellation with N grains and characterized by its (bulk) volume v_{Ω} as well as the n_{F} GB facets with surface areas A_i and normals $\underline{\underline{n}}_i$. In our model, the total volume V is given as the sum of bulk volume v_{Ω} and the implicitly represented GB volume v_{GB} . This yields the volume fractions of bulk f_{Ω} and GB f_{GB} :

$$v_{\text{GB}} = \sum_{i=1}^{n_{\text{F}}} 2hA_i = 2hA, \quad f_{\Omega} = \frac{v_{\Omega}}{V}, \quad f_{\text{GB}} = \frac{v_{\text{GB}}}{V}. \quad (33)$$

Note that the volume fractions compensate the additional GB volume and satisfy $f_{\Omega} + f_{\text{GB}} = 1$.

In order to quantify the anisotropy in a microstructure, we furthermore define a second-order structural tensor

$$\underline{\underline{S}}_2 = \sum_{i=1}^{n_{\text{F}}} \frac{A_i}{A} \underline{\underline{n}}_i \otimes \underline{\underline{n}}_i \in \mathbb{R}^{3 \times 3} \quad \text{with } A = \sum_{i=1}^{n_{\text{F}}} A_i. \quad (34)$$

The limits of this tensor for extreme but characteristic geometries can be derived from the extension of the discrete sum of interface facets to a surface integral on a corresponding ellipsoid. For reference, the results for perfectly isotropic geometries (as it appears in the limit case of $N \rightarrow \infty$), prolate 'needle'-like grains and oblate 'flake-like' grains are given:

$$\underline{\underline{S}}_2^{\text{sphere}} = \begin{bmatrix} 1/3 & 0 & 0 \\ 0 & 1/3 & 0 \\ 0 & 0 & 1/3 \end{bmatrix}, \quad \underline{\underline{S}}_2^{\text{prolate}} \rightarrow \begin{bmatrix} 1/2 & 0 & 0 \\ 0 & 1/2 & 0 \\ 0 & 0 & 0 \end{bmatrix}, \quad \underline{\underline{S}}_2^{\text{oblate}} \rightarrow \begin{bmatrix} 0 & 0 & 0 \\ 0 & 0 & 0 \\ 0 & 0 & 1 \end{bmatrix}. \quad (35)$$

The corresponding spheroids are shown in Figure 3. Note that the prolate and oblate limit cases correspond to the ratio of the semi-axis going to infinity.

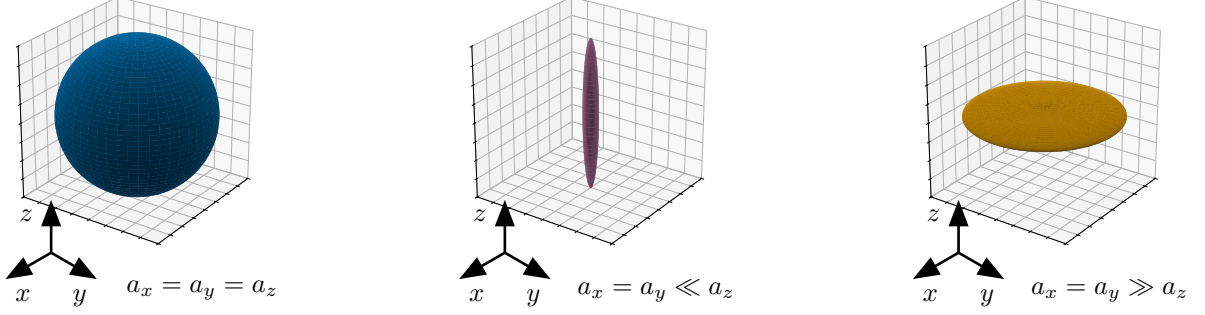


Figure 3: Limit cases of a spheroid with semi-axis lengths a_x, a_y, a_z : sphere, prolate (needle-like) and oblate (flake-like).

2.4.2 Effective diffusion coefficients

Following the framework of linear computational homogenization [46], we introduce the following notation for phase-wise volume averages in bulk and GB:

$$\langle [\cdot] \rangle_{\Omega} := \frac{1}{v_{\Omega}} \int_{\Omega} [\cdot] dV, \quad (36)$$

$$\langle [\cdot] \rangle_{\parallel} := \frac{1}{v_{\text{GB}}} \int_A \int_{-h}^h (\underline{\mathbf{I}} - \underline{\mathbf{n}} \otimes \underline{\mathbf{n}}) [\cdot] d\zeta_n dS, \quad \langle [\cdot] \rangle_{\perp} := \frac{1}{v_{\text{GB}}} \int_A \int_{-h}^h (\underline{\mathbf{n}} \otimes \underline{\mathbf{n}}) [\cdot] d\zeta_n dS. \quad (37)$$

For an arbitrary geometry and set of material parameters the global system in eq. (32) is solved for different right-hand sides induced by the imposed unit gradients $\underline{\bar{g}}_k = \underline{e}_k$ ($k = 1, 2, 3$) to obtain the corresponding fluctuation fields. The phase-wise volume averages $\langle \underline{g}_k \rangle_{[\cdot]}$ have contributions from the imposed gradient field and the resulting fluctuation field:

$$\langle \underline{g}_k \rangle_{\Omega} = \underline{\bar{g}}_k + \langle \nabla \tilde{c}_k \rangle_{\Omega}, \quad \langle \underline{g}_k \rangle_{\parallel} = (\underline{\mathbf{I}} - \underline{\mathbf{S}}_2) \underline{\bar{g}}_k + \langle \nabla \tilde{c}_k \rangle_{\parallel}, \quad \langle \underline{g}_k \rangle_{\perp} = \langle \nabla \tilde{c}_k \rangle_{\perp}. \quad (38)$$

Note that $\langle \underline{g}_k \rangle_{\perp}$ is not affected by the imposed gradient since all nodes in the thickness direction of the interface share the same physical position due to the collapsed interface representation. To compute the averaged gradients of the fluctuation fields, we define phase-wise operators $\mathbb{G}_{[\cdot]} \in \mathbb{R}^{3 \times d}$ to obtain the gradient field integrated over the domain. These will be of use later. This results in

$$\langle \nabla \tilde{c}_k \rangle_{\Omega} = \frac{1}{v_{\Omega}} \mathbb{G}_{\Omega} \tilde{c}_k \quad \text{with } \mathbb{G}_{\Omega} = \sum_{i=1}^{n_{\text{el}}^{\Omega}} \sum_{j=1}^{n_{\text{GP}}^{\text{T10}}} \omega_j^{(i)} \underline{\mathbf{B}}_{\Omega}^{(i)}(\zeta_j) \underline{\mathbf{L}}_{\Omega}^{(i)}, \quad (39)$$

$$\langle \nabla \tilde{c}_k \rangle_{\parallel} = \frac{1}{v_{\text{GB}}} \mathbb{G}_{\parallel} \tilde{c}_k \quad \text{with } \mathbb{G}_{\parallel} = \frac{2h}{6} \sum_{i=1}^{n_{\text{el}}^{\text{GB}}} \sum_{j=1}^{n_{\text{GP}}^{\text{C18}}} \nu_j^{(i)} \left[\underline{\mathbf{B}}_{\text{P2}}^{(i)}(\zeta_{t(j)}) \quad 4\underline{\mathbf{B}}_{\text{P2}}^{(i)}(\zeta_{t(j)}) \quad \underline{\mathbf{B}}_{\text{P2}}^{(i)}(\zeta_{t(j)}) \right] \underline{\mathbf{L}}_{\text{GB}}^{(i)}, \quad (40)$$

$$\langle \nabla \tilde{c}_k \rangle_{\perp} = \frac{1}{v_{\text{GB}}} \mathbb{G}_{\perp} \tilde{c}_k \quad \text{with } \mathbb{G}_{\perp} = \sum_{i=1}^{n_{\text{el}}^{\text{GB}}} \sum_{j=1}^{n_{\text{GP}}^{\text{C18}}} \nu_j^{(i)} \underline{\mathbf{n}}_i \left[-\underline{\mathbf{N}}_{\text{P2}}^{(i)}(\zeta_{t(j)}) \quad \underline{\mathbf{0}} \quad \underline{\mathbf{N}}_{\text{P2}}^{(i)}(\zeta_{t(j)}) \right] \underline{\mathbf{L}}_{\text{GB}}^{(i)}. \quad (41)$$

The overall volume average of the microscopic gradients and fluxes based on $\underline{\bar{g}}_k$ are then given as

$$\underline{\mathbf{G}}_k = f_{\Omega} \langle \underline{g}_k \rangle_{\Omega} + f_{\text{GB}} \left(\langle \underline{g}_k \rangle_{\parallel} + \langle \underline{g}_k \rangle_{\perp} \right), \quad (42)$$

$$\underline{\mathbf{Q}}_k = - \left(f_{\Omega} D_{\Omega} \langle \underline{g}_k \rangle_{\Omega} + f_{\text{GB}} \left(D_{\parallel} \langle \underline{g}_k \rangle_{\parallel} + D_{\perp} \langle \underline{g}_k \rangle_{\perp} \right) \right). \quad (43)$$

Stacking $\underline{\mathbf{G}}_k$ and $\underline{\mathbf{Q}}_k$ for all three load cases ($k = 1, 2, 3$)

$$\underline{\underline{\mathbf{G}}} = [\underline{\mathbf{G}}_1 \quad \underline{\mathbf{G}}_2 \quad \underline{\mathbf{G}}_3] \in \mathbb{R}^{3 \times 3}, \quad \underline{\underline{\mathbf{Q}}} = [\underline{\mathbf{Q}}_1 \quad \underline{\mathbf{Q}}_2 \quad \underline{\mathbf{Q}}_3] \in \mathbb{R}^{3 \times 3} \quad (44)$$

yields the effective diffusion tensor on mesoscale

$$\underline{\underline{D}} = -\underline{Q}\underline{G}^{-1} \in \mathbb{R}^{3 \times 3}. \quad (45)$$

In the case where $D_\Omega = D_\parallel = D_\perp$ the definition of the volume fractions in eq. (33) compensates the additional GB volume and yields $\underline{Q} = -D_\Omega \underline{G}_k$ and therefore $\underline{\underline{D}} = D_\Omega \underline{I}$. Hence, the GB does not influence the response in this case.

2.4.3 Voigt-Reuss bounds

Analytical bounds for the effective material response, i.e., the coefficients of the effective diffusion tensor $\underline{\underline{D}}$, exist, which are given by the weighted arithmetic and harmonic mean of the phase-specific material properties. In the following we refer to them as (upper) Voigt [24] and (lower) Reuss [25] bound $\underline{\underline{D}}_V$ and $\underline{\underline{D}}_R$ as commonly done in mechanics². With the assumptions of an isotropic bulk (Section 2.1) and a transversely isotropic GB (Assumption [A4]) as well as the geometry-specific characteristic quantities from Section 2.4.1 expressions for both bounds can be derived:

$$\underline{\underline{D}}_V = f_\Omega D_\Omega \underline{I} + f_{GB} D_\parallel \left(\frac{D_\perp - D_\parallel}{D_\parallel} \underline{S}_2 + \underline{I} \right), \quad \underline{\underline{D}}_R = \left(\frac{f_\Omega}{D_\Omega} \underline{I} + \frac{f_{GB}}{D_\parallel} \left(\frac{D_\parallel - D_\perp}{D_\perp} \underline{S}_2 + \underline{I} \right) \right)^{-1}. \quad (46)$$

Due to the transversely isotropic properties of the GB the bounds exhibit a dependence on the structural tensor \underline{S}_2 as defined in eq. (34), i.e., the anisotropy of the geometry governs the anisotropy of the bounds. For $D_\Omega = D_\parallel = D_\perp$ the bounds yield a sharp estimate with $\underline{\underline{D}}_V = \underline{\underline{D}}_R$. In the limit case of an isotropic structure ($N \rightarrow \infty$) the bounds converge to

$$\underline{\underline{D}}_V \rightarrow \left(f_\Omega D_\Omega + f_{GB} \frac{D_\perp + 2D_\parallel}{3} \right) \underline{I}, \quad \underline{\underline{D}}_R \rightarrow \left(\frac{f_\Omega}{D_\Omega} + f_{GB} \frac{D_\parallel + 2D_\perp}{3D_\perp D_\parallel} \right)^{-1} \underline{I}. \quad (47)$$

In order to derive a relative scaling of the effective diffusion tensor $\underline{\underline{D}}$ with respect to the Voigt-Reuss bounds, we follow the derivation introduced in the context of the Voigt-Reuss net [58]. It is also roughly outlined in the following: The effective diffusion tensor $\underline{\underline{D}}$ for an arbitrary configuration needs to satisfy the derived Voigt and Reuss bounds in the following sense:

$$\underline{y}^\top \left(\underline{\underline{D}}_V - \underline{\underline{D}}_R \right) \underline{y} \geq \underline{y}^\top \left(\underline{\underline{D}} - \underline{\underline{D}}_R \right) \underline{y} \geq 0 \quad \forall \underline{y} \in \mathbb{R}^3. \quad (48)$$

Performing a Cholesky decomposition on the symmetric and positive-definite difference $\underline{\underline{D}}_V - \underline{\underline{D}}_R$

$$\underline{\underline{D}}_V - \underline{\underline{D}}_R = \underline{\underline{L}} \underline{\underline{L}}^\top \quad \text{i.e., } \underline{\underline{L}} = \left(\underline{\underline{D}}_V - \underline{\underline{D}}_R \right)^{1/2} \quad (49)$$

allows to rewrite the bounding relations as

$$\underline{z}^\top \underline{z} \geq \underline{z}^\top \underline{\underline{L}}^{-\top} \left(\underline{\underline{D}} - \underline{\underline{D}}_R \right) \underline{\underline{L}}^{-1} \underline{z} \geq 0 \quad (50)$$

if $\underline{y} = \underline{\underline{L}}^{-1} \underline{z}$ with $\underline{z} \in \mathbb{R}^3$ is chosen. This can only be satisfied if the following eigendecomposition with restrictions exists:

$$\underline{\underline{L}}^{-\top} \left(\underline{\underline{D}} - \underline{\underline{D}}_R \right) \underline{\underline{L}}^{-1} = \underline{\underline{Q}}^\top \underline{\underline{\Lambda}} \underline{\underline{Q}} \quad \text{with } \underline{\underline{\Lambda}} = \text{diag}(\lambda_i), \quad \lambda_i \in [0, 1] \quad (i \in \{1, 2, 3\}). \quad (51)$$

The eigenvalues λ_i might be used as a direct scalar measure to describe the relation of the material response to Voigt (close to 1) and Reuss (close to 0). This will be used for the study in Section 4.4. Note that the presented parametrization is inverse to the one in the Voigt-Reuss net [58].

²Note that field-specific alternative terms for the same bounds exist such as the Wiener bounds [23] in permittivity.

2.5 Affine parameter dependence and dimensionless formulation

The system of equations stated in eq. (32) exhibits a dependence on the diffusion coefficients D_Ω , D_\parallel , and D_\perp as well as the GB thickness parameter h . In the following, we further parameterize the geometry with respect to a reference geometry of edge length l_0 and introduce a uniform scaling by l/l_0 . For a reference diffusion coefficient D_0 and the reference length l_0 , the following five-dimensional parameter set of dimensionless scaling factors is obtained:

$$\pi_\Omega = \frac{D_\Omega}{D_0}, \quad \pi_\parallel = \frac{D_\parallel}{D_0}, \quad \pi_\perp = \frac{D_\perp}{D_0}, \quad \pi_h = \frac{h}{l_0}, \quad \pi_l = \frac{l}{l_0}. \quad (52)$$

Interestingly, the Buckingham Pi Theorem [59] yields only two independent variables for the five-dimensional parametrization defined in eq. (52). In fact, the domain-specific stiffness matrices in eq. (32) exhibit an affine dependence on the material and geometrical parameters:

$$\underline{K}_\Omega^e = \pi_\Omega \pi_l \underline{K}_\Omega^{e,0}(D_0, l_0) \quad \underline{K}_\parallel^e = \pi_\parallel \pi_h \underline{K}_\parallel^{e,0}(D_0, l_0), \quad \underline{K}_\perp^e = \frac{\pi_\perp \pi_l^2}{\pi_h} \underline{K}_\perp^{e,0}(D_0, l_0). \quad (53)$$

Quantities from the reference geometry are indicated by the superscript 0. A more detailed derivation can be found in Appendix B. By introducing the two intrinsic parameters

$$\Pi_\parallel = \frac{\pi_\parallel \pi_h}{\pi_\Omega \pi_l}, \quad \Pi_\perp = \frac{\pi_\perp \pi_l}{\pi_\Omega \pi_h} \quad (54)$$

for each configuration $[\pi_\Omega, \pi_\parallel, \pi_\perp, \pi_h, \pi_l]$ the system of equations defined in eq. (32) can be rewritten as

$$\left(\underline{K}_\Omega^0 + \Pi_\parallel \underline{K}_\parallel^0 + \Pi_\perp \underline{K}_\perp^0 \right) \tilde{c} = r_\Omega^0 + \Pi_\parallel r_\parallel^0 + \Pi_\perp r_\perp^0. \quad (55)$$

Hence, the intrinsic dimension of the problem is two. In summary, all configurations $\underline{\pi} = [\pi_\Omega, \pi_\parallel, \pi_\perp, \pi_h, \pi_l]$ that lead to the same $\underline{\Pi} = [\Pi_\parallel, \Pi_\perp]$ have the same discrete solution \tilde{c} for the fluctuation field.

While the fluctuation field and the corresponding integrated gradients in eq. (38) have a lower intrinsic dimension, this does not hold for the flux field and the effective diffusivity tensor (see Appendix B.2). They scale directly with the absolute values of the phase-specific diffusion coefficients and volume fractions, which depend on the ratio of π_h/π_l . However, the computational effort for these postprocessing steps is insignificant as it reduces to scalar pre-factors, given the integrated gradients. The number of system configurations for which eq. (55) needs to be solved is considerably reduced.

Remark 5. *The lengths l_0 and l represent the edge length of the used unit cell. They directly relate to the grain size. By keeping $\pi_\Omega, \pi_\parallel, \pi_\perp$ and π_h constant but varying π_l a direct investigation of the grain size is possible.*

3 A 2D validation example

3.1 Setup

In order to verify the choice of a second-order approximation for the concentration profile across the GB, a simplified two-dimensional example is considered. In this case, a fully resolved representation of the GB domain is feasible and can be used as a reference solution. As depicted in Figure 4 the geometry consists of a square-shaped grain of sides with length L_{grain} in a periodic setting that is separated from itself by a GB layer of thickness $2h$.

In the following we aim to compare the resulting fluctuation fields as well as the effective properties for the collapsed interface elements and for a fully resolved GB. Note that a fixed bulk volume yields different total geometry volumes (and, therefore, volume fractions) due to the implicit representation of the GB in the collapsed case:

$$v_{\text{bulk}}^{\text{full}} = L_{\text{grain}}^2, \quad v_{\text{GB}}^{\text{full}} = 2(L_{\text{grain}} \cdot 2h) + (2h)^2, \quad v_{\text{RVE}}^{\text{full}} = L_{\text{grain}}^2 + 4L_{\text{grain}}h + 4h^2, \quad (56)$$

$$v_{\text{bulk}}^{\text{coll}} = L_{\text{grain}}^2, \quad v_{\text{GB}}^{\text{coll}} = 2(L_{\text{grain}} \cdot 2h), \quad v_{\text{RVE}}^{\text{coll}} = L_{\text{grain}}^2 + 4L_{\text{grain}}h. \quad (57)$$

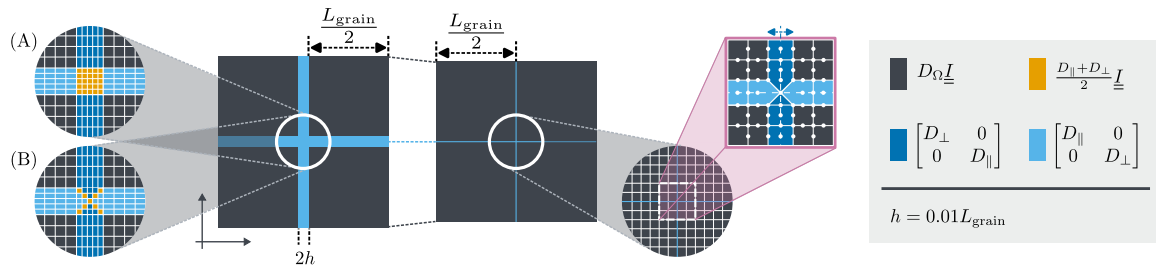


Figure 4: Sketch of the compared setups using a fully-resolved GB (left) and the proposed collapsed representation (right). Geometrical features and assigned material properties are given as well. For the fully-resolved case the two possible parametrizations of the junction domain (A) and (B) are shown. In this case, the GB width $2h$ is chosen to be two percent of the grain size L_{grain} .

Furthermore, the parametrization of the GB junction at the center is non-trivial in the fully-resolved case. Hence, we investigate two reasonable variants as shown on the left of Figure 4:

- (A) isotropic diffusion behavior in the junction domain (i.e., arithmetic average of D_{\parallel} and D_{\perp}),
- (B) junction domain divided into triangles with properties inherited from neighboring GB segments.

With the values given in Figure 4 the volume fractions for the fully-resolved and the collapsed setup are $f_{\text{GB}}^{\text{full}} \approx 3.88\%$ and $f_{\text{GB}}^{\text{coll}} \approx 3.85\%$ which are values unlikely to be seen for realistic microstructures in which the GB contributes lesser volume. The deviation between the full and the collapsed model stems from the GB junction domain that we do not account for in the collapsed case. However, in realistic applications with $h \ll L_{\text{grain}}$, the h^2 -term in eq. (57) becomes negligible, justifying the validity of this choice.

Following the model description above, the problem is complemented with periodic boundary conditions, and one node is fixed to an arbitrary concentration. We impose a macroscopic gradient \bar{q} as a driving force.

3.2 Approximation quality of the proposed concentration profile within the interface

In the following, we want to investigate whether the assumed second-order ansatz is sufficient to capture the relevant features of the concentration profile across the GB and how well the collapsed model approximates the fully resolved results. We choose the gradient $\bar{q} = [4/5 \quad 3/5]^T$ to analyze the transversely isotropic GB parametrization. In Figure 5, the concentration profiles for all three approaches at characteristic positions close and further away from the junction are shown. In addition, a least-squares fit of a second-order polynomial is added for the two fully resolved cases (A) and (B).

The choice of the parametrization for the junction clearly affects the resulting concentration profile in the anisotropic case. While the profiles resulting from approach (A) are perfectly captured by a second-order fit in all cases, setup (B) exhibits higher-order nonlinearity close to the junction. Hence, considering at least one term of even order is essential to properly capture the diffusion within the GB while the neglect of higher-order terms is a reasonable assumption.

The fully-resolved concentration profiles are compared with the second-order reconstruction of the collapsed representation: Note that all subplots in Figure 5 exhibit a different scaling of the concentration axis. Furthermore, the deviation from the concentration value of setup (A) at position $-h$ is displayed rather than the actual concentration values to allow for a better comparison. The jump in concentration captured by the proposed model aligns very well with the one of setup (B). However, deviations between both models can be observed at the junction close to the GB center line (cases **b**, **c**). For the direct vicinity of the junction the collapsed interface elements cause inaccuracies by construction: The entire behavior within the junction is only modeled by a single shared middle plane node. In setups with large concentration jumps (e.g., caused by $D_{\perp} \ll D_{\Omega}$) this node will most likely represent an average of the surrounding top and bottom nodes of all affected interface elements. On average, this expected behavior is mitigated since an overestimation at position **b** will always cause an underestimation at position **c** due to the point symmetry of the concentration profiles.

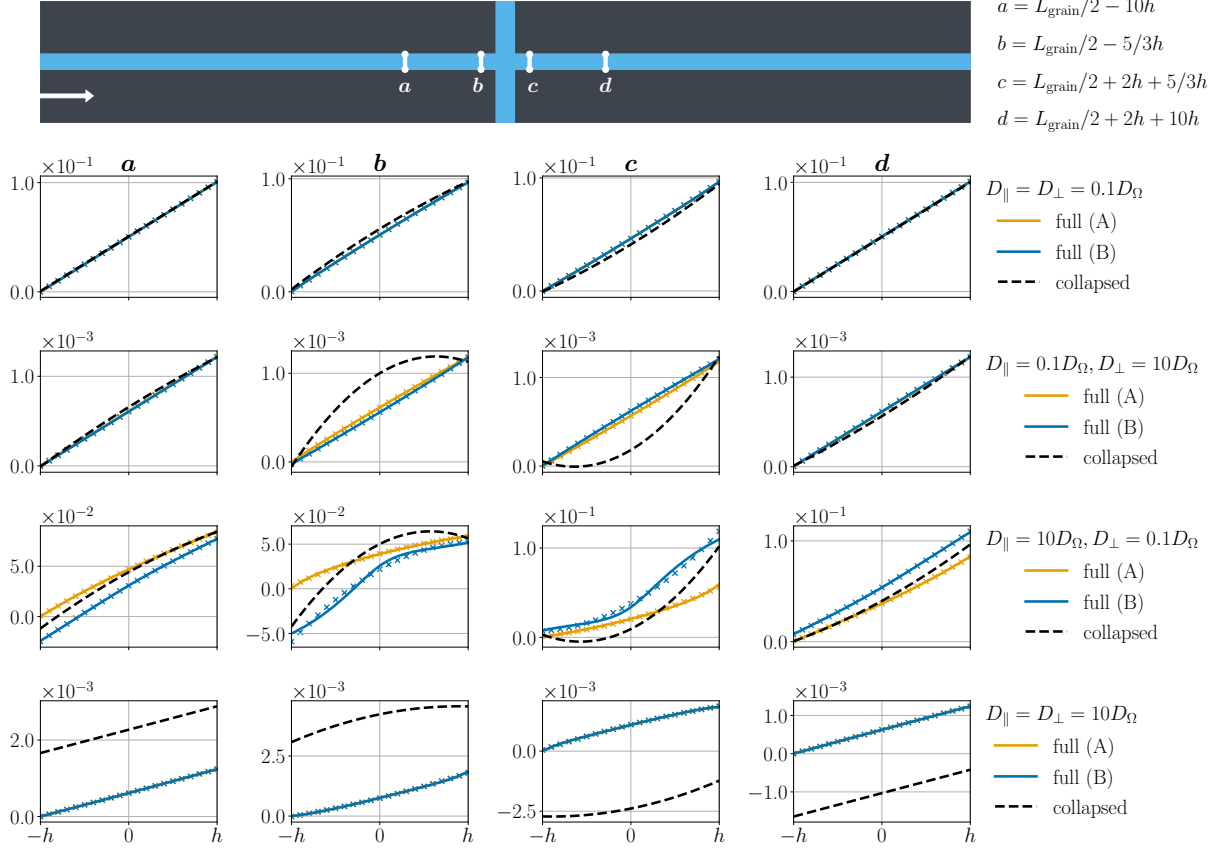


Figure 5: (Shifted) concentration profiles across the GB in the positions a , b , c and d highlighted in the schematic at the top: Each row represents a different parameter configuration (D_{\parallel}/D_{Ω} , D_{\perp}/D_{Ω}). For the isotropic cases (top and bottom row) setup (A) and (B) coincide. Least-squares second-order polynomial fits for the setups (A) and (B) are given by the \times -markers in the respective color. The matching results for the proposed collapsed GB representation are shown for reference. For the sake of an easy comparison, the absolute concentration values were shifted such that the concentration value of setup (A) at position $-h$ resembles the zero value.

It is noteworthy that Fisher-like transport models [35] with reduced representations cannot capture any of the partially significant concentration jumps across the GB nor the detailed concentration profile. Furthermore, the independent variation of D_{\parallel} and D_{\perp} clearly affects the resulting concentration field. Hence, a restriction to a single diffusion coefficient for the GB domain (either to account for jumps or for in-plane transport), as done in most GB diffusion models, is an oversimplifying assumption. The detailed effects will be studied in Section 4.

3.3 Approximation accuracy in effective properties

To obtain the effective diffusion tensor $\overline{\underline{D}}$ we keep the geometrical setup from Figure 4 fixed and solve the described diffusion problem for the two uniaxial load cases \overline{g}_k ($k = 1, 2$). Due to the symmetric setup, we find $\overline{\underline{D}} = \overline{\underline{D}}^T$. As before the ratios of material parameters D_{\parallel}/D_{Ω} and D_{\perp}/D_{Ω} are varied.

For the case of $D_{\Omega} = D_{\parallel} = D_{\perp}$ the effective diffusion coefficient $\overline{\underline{D}}$ is found to perfectly recover a homogeneous material. For the sake of brevity, we omit a detailed interpretation of the dependence of $\overline{\underline{D}}$ on the parameter space here and refer to Section 4.4 instead. Only the deviation in the effective diffusion coefficient between the fully-resolved setups (A) and (B) and the collapsed GB representation are considered in Figure 6a and 6b where a sound agreement was found (deviations $\leq 1\%$). The deviations of both setups are similar except for the domain where $D_{\parallel} > D_{\Omega}$ and $D_{\perp} < D_{\Omega}$: Figure 6a mildly underestimates $\overline{\underline{D}}$ while Figure 6b yields a slight overestimation. This implies that in this regime, both

fully-resolved setups differ, and the proposed model yields a meaningful in-between estimate. While the maximum deviation in (A) is larger than in (B), it exhibits better agreement on average.

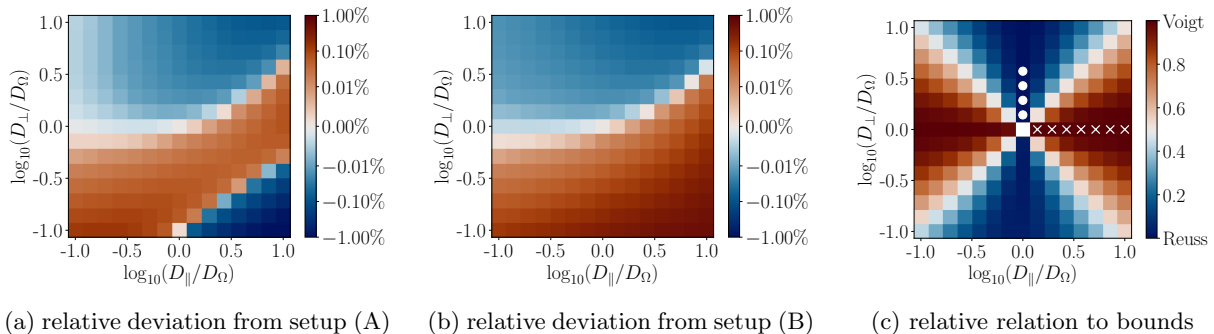


Figure 6: **(a)+(b)**: Relative deviation in the effective diffusion coefficient \bar{D} of the proposed model with respect to the fully resolved setups (A) and (B). Positive numbers indicate an overestimation and negative numbers indicate an underestimation. For the trivial case of $D_{\parallel} = D_{\perp} = D_{\Omega}$ perfect agreement is found. **(c)**: Relation of the effective diffusion coefficient from the proposed model to the Voigt-Reuss bounds. Violations of the Voigt and Reuss bound are marked with \times and \circ , respectively.

For the given symmetric 2D setup the relation to the Voigt-Reuss bounds as stated in (51) reduces to:

$$\lambda(\bar{D}) = \frac{\bar{D} - D_{\text{R}}}{D_{\text{V}} - D_{\text{R}}}. \quad (58)$$

We recall that $\lambda = 1$ corresponds to $\bar{D} = D_{\text{V}}$ and $\lambda = 0$ implies that $\bar{D} = D_{\text{R}}$. Note that the Reuss bounds differ between the fully-resolved setups (A) and (B) by up to 0.5% whereas the Voigt bounds are identical. For the scaling of the collapsed setup, as shown in Figure 6c the Reuss bound of setup (A) was used. For some configurations, slight (numerical) violations of the bounds are observed. This can be explained by the required approximations resulting from the proposed collapsed element and the corresponding artificially added volume as well as the ambiguity of the 'correct' Reuss bound. However, these violations remain in a negligible range of less than 0.1%.

In summary, the validation example proves that the collapsed interface model resembles the fully-resolved setups well in a global sense. Local deviations appear mainly close to the junction where they are expected by construction. However, in these places, the results for the parametrizations (A) and (B) differ as well. For the computation of the effective diffusion coefficients, the volume averaging removes the majority of the point symmetric deviations and leads to a very good agreement with the fully resolved setups. In the following, the second-order ansatz is, therefore, used as a justified approximation choice for the GB profile.

4 Analysis of ion diffusion in a polycrystalline setup

4.1 Objectives

For the present study, an arbitrary geometry is chosen, which is constructed as a Voronoi tessellation with 100 grains. Geometry and bulk mesh were generated using the software *nepher* [56,60]. The interface elements were added by extending standard approaches for inserting cohesive elements [61]. The structural tensor of the considered geometry as defined in eq. (34) and its eigenvalues λ_i

$$\underline{\underline{S}}_2 \approx \begin{bmatrix} 0.3352 & 0.0017 & 0.0002 \\ 0.0017 & 0.3293 & 0.0033 \\ 0.0002 & 0.0033 & 0.3355 \end{bmatrix} \quad \frac{\lambda_1}{\lambda_0} \approx 0.9936 \quad \frac{\lambda_2}{\lambda_0} \approx 0.9713 \quad (59)$$

justify the choice of this setup as a representative microstructure with a nearly isotropic structure. The considered discretization consists of 1,181,055 volume elements for the bulk and 78,074 cohesive elements for the GBs resulting in 1,951,614 DOFs.

Note that the volume fraction of the setup can be varied artificially for a fixed geometry by controlling the relation between the GB thickness parameter and geometry length scale h/l which is one of the key advantages of the collapsed GB representation. To comply with the assumption of a thin GB that forms the foundation of the introduced thickness-collapsed GB model, we focus on systems with a small GB volume fraction of $f_{\text{GB}} < 10\%$. In accordance with the results summarized in the atomistic study of Ou et al. [11] and with an additional margin to study more extreme setups, we consider $D_{\parallel}, D_{\perp} \in [0.01 D_{\Omega}, 100 D_{\Omega}]$ to be a realistic range of GB diffusion coefficient ratios.

Given the proposed model, we now aim to explore the qualitative and quantitative characteristics of the resulting ion diffusion and their dependence on the parameters $\underline{\pi}$ as introduced in eq. (52). An in-depth understanding of these effects requires insight into the local diffusion mechanisms as well as the emerging global diffusion regimes. Through meaningful metrics and supporting visualizations we underline the features that can be captured by the proposed model. Special attention is given to the impact of GBs. The study is based on and structured by the following guiding questions:

1. **Localizing diffusion:** How do GB properties deviating from the bulk properties affect the preferred paths of ion transport?
2. **Characterizing transport in GBs:** How do local transport mechanisms form a global diffusion regime?
3. **Quantifying the impact of GB transport:** To what extent can the consideration of GB transport enhance or limit the overall diffusivity of the polycrystalline material?

Relevant aspects and findings are discussed in the subsequent sections. The previously introduced reference geometry is used for all of the presented results.

4.2 Localizing diffusion

As stated in Section 2.2 the material response converges to the one of a homogeneous bulk material with idealized interfaces not only in case of a vanishing GB thickness ($h \rightarrow 0$) but also if $D_{\perp} \gg D_{\Omega}$ and $D_{\parallel} \ll D_{\Omega}$. Streamlines for the flux field as depicted in Figure 7a are parallel to the ones of the imposed gradient field inside of the bulk. The flux magnitude remains uniform. The distribution of accumulated flux across bulk and GB in Figure 8 underlines that the overall transport is clearly bulk-dominated in this case. In general, however, the flux distribution over the domains exhibits a strong dependence on the GB parameters: The diffusion coefficient in normal direction D_{\perp} has a limiting character, i.e., for $D_{\perp} \ll D_{\Omega}$ ion diffusion in the bulk is severely hindered compared to the bulk-like case. Opposed to that, $D_{\parallel} \gg D_{\Omega}$ leads to a significant enhancement of the in-plane flux and a slight increase of the absolute normal transport (although the relative share is reduced). The accumulated flux in the bulk, however, remains unaffected. Hence, increasing D_{\parallel} introduces additional diffusion paths.

When taking a closer look at the local flux field in the bulk, the streamlines in Figure 7 show how the diffusion paths starting in the same seed points in the bulk vary solely depending on the material properties of the GBs. In contrast to the bulk-like case, locally varying flux fields and diffusion paths are observed for all other limit cases: If we allow for additional diffusion along the GBs (i.e., configuration in Figure 7b) or introduce GBs with a hindering and limiting effect (i.e., configuration in Figure 7c) the magnitude of the flux clearly reflects the distribution and shape of the grains and of the GBs. We obtain discontinuities in the magnitude of the flux across the GBs and slightly deviating diffusion paths.

The case in Figure 7d with enhanced transport along the GB but limited ability to cross the GB deserves special attention. The diffusion paths within the bulk domain are completely governed by the local structure and deviate heavily from the direction of the imposed gradient. Some of the streamlines exhibit an oscillating behavior along certain GB facets. Note that these streamlines are only based on the flux field of the bulk domain and do, therefore, not reflect the transport behavior within the GBs for now. This, however, underlines the need to thoroughly investigate the detailed transport behavior within the GBs as we will do in Section 4.3.

While the streamlines help gain a feel for different regimes, they are of limited use when it comes to comparing potentially very similar parameter configurations. The relevant features enhanced by the streamlines comprise local variations in flux magnitude as well as the orientation of the flux. We, therefore,

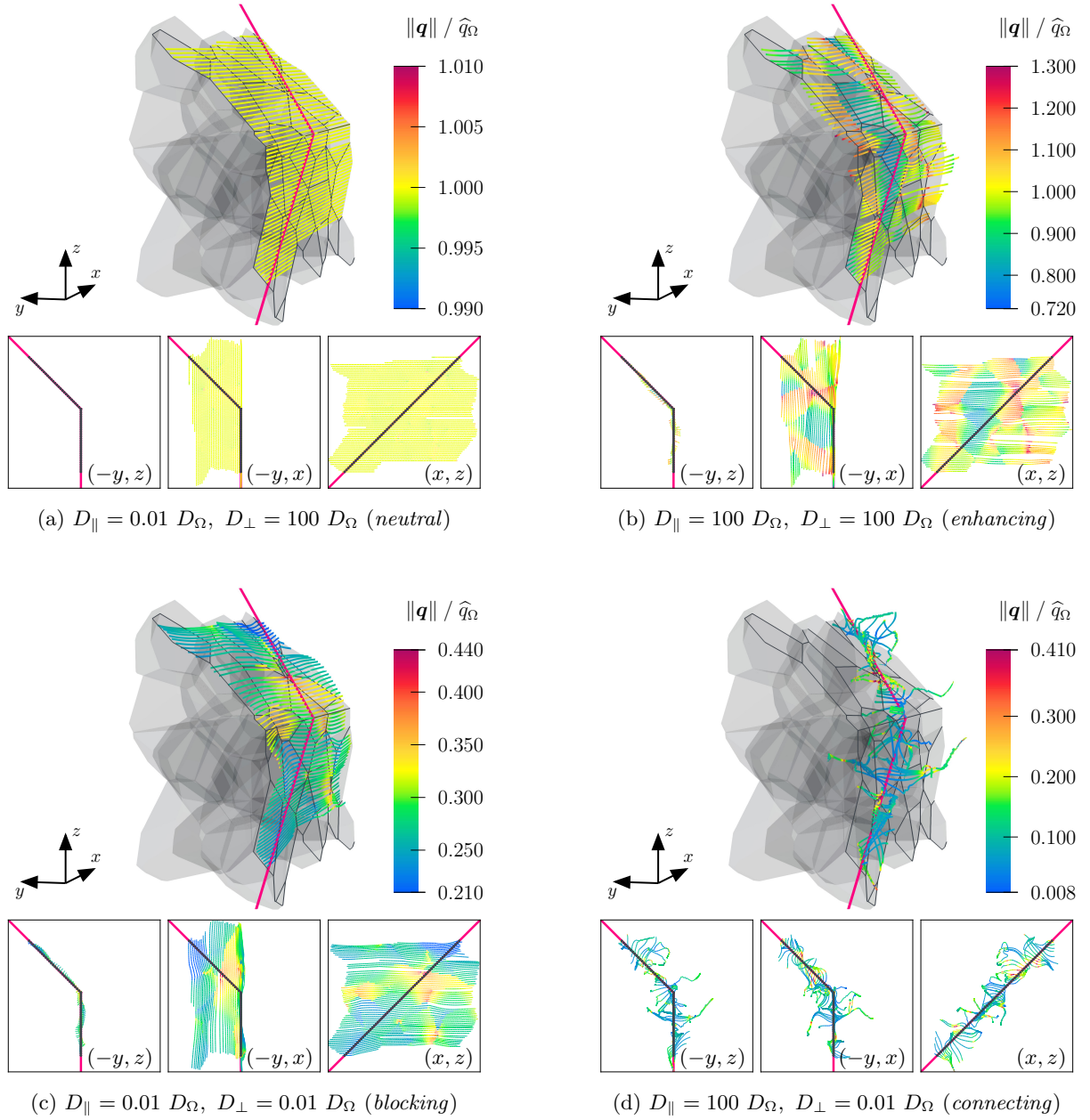


Figure 7: Selected streamlines stemming from the dedimensionalized bulk flux field are shown for the case of an imposed gradient \bar{g} along the x -axis. The flux is dedimensionalized with $\hat{q}_{\Omega} = \|-D_{\Omega}\bar{g}\|$. The seeds of the streamlines were equidistantly spaced along the pink lines. For a better comparison the respective projections (of a selection of streamlines) onto the planes of the coordinate system are given as well. The relative GB thickness parameter was fixed to $h = 0.0032l$ for all configurations, resulting in a volume fraction of $f_{\text{GB}} \approx 7.80\%$. The material parameters for the GB are given for the respective subplots together with the transport regimes introduced in Table 1. The color map was chosen to highlight the local differences in the flux magnitude.



Figure 8: Split of the overall magnitude of integrated flux in bulk domain (gray area Ω) as well as in-plane and normal direction in the GB (blue area) for varying material parameters (D_{\parallel}/D_{Ω} , D_{\perp}/D_{Ω}) and an imposed gradient in global x -direction. We fixed $h = 0.0032l$ for all configurations (i.e., $f_{\text{GB}} \approx 7.80\%$). The yellow numbers represent the relative change in total flux with respect to the configuration on the top left. The split of the total flux in bulk and the two GB contributions is given in the white boxes.

define the second moment of the flux field in the bulk domain Ω as

$$\underline{\underline{R}} = \frac{1}{|\Omega|} \int_{\Omega} \underline{q} \otimes \underline{q} dV - \langle \underline{q} \rangle_{\Omega} \otimes \langle \underline{q} \rangle_{\Omega} \quad (60)$$

accounting for the flux volume average $\langle \underline{q} \rangle_{\Omega}$. The second moment corresponds to the covariance matrix of the 3D ion flux field, where the diagonal entries directly correspond to the variance in the flux along the respective coordinate axes. Hence, we propose it as a suitable metric for directly comparing configurations. Note that the computation of the metric is performed using numerical integration in this context. In Figure 9, the ellipsoids corresponding to $\underline{\underline{R}}$ of different configurations are shown in order to visually enhance the directions of the largest variation. Note that only D_{\perp}/D_{Ω} was varied for these visualizations. The larger the components of $\underline{\underline{R}}$ are, the more local variations appear. In the case of an (almost) perfectly uniform flux field as displayed in Figure 7a for the bulk-like regime, all components of $\underline{\underline{R}}$ should tend to zero.

In all displayed cases, the eigenvector with the dominating eigenvalue is close to the direction of loading, i.e., the x -axis in this case, as suggested by Figure 7. Therefore, any local deviation in magnitude and/or direction leads to a larger absolute variance along this direction. The general shape of the ellipsoids is close to a spheroid, as can be seen in the middle perspective, due to the close-to isotropic property of the structural tensor in eq. (59).

For $D_{\perp} \geq D_{\Omega}$, the eigenvalues show only minor variations. Therefore, the two innermost ellipsoids are hard to distinguish. The most relevant change is that the ellipsoid becomes more similar to a sphere, which implies that the flux variance depends less on the loading direction. This also causes an intersection of those two ellipsoids. For $D_{\perp} < D_{\Omega}$ the magnitude of the eigenvalues grows rapidly, underlining how the limited ability to enter and leave the GB forces ions to take alternative routes and detours within the bulk as well as the GB. This also causes an increased variance in the non-loading directions.

Based on the observations presented in this section, we define four regimes of transport based on the impact of GBs as shown in Table 1. In the following, we use these terms when referring to the four limit

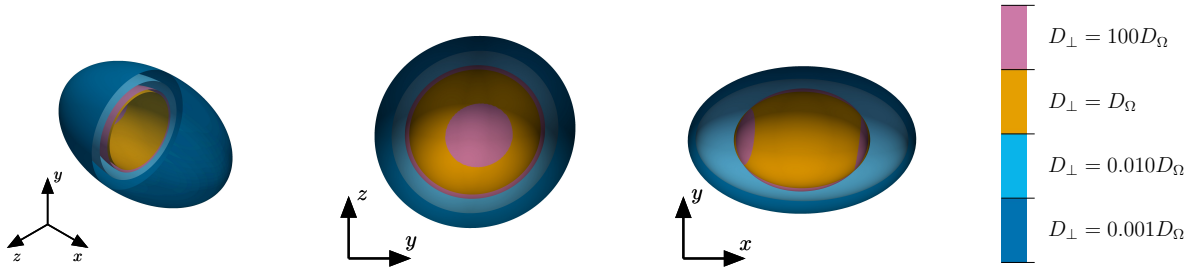


Figure 9: Ellipsoids representing the relative second moment of the dedimensionalized flux-field in the bulk domain as defined in eq. (60) for an imposed gradient in x -direction $\bar{g} = [1 \ 0 \ 0]$ and different parameter configurations. The ellipsoids are constructed based on the eigenvectors of \underline{R} scaled with the square roots of the corresponding eigenvalues. We fixed $D_{\parallel} = 10 D_{\Omega}$ for all cases and varied D_{\perp}/D_{Ω} as shown in the color bar. The shown cuts and perspectives highlight the intersections of the latter two ellipsoids.

cases in order to keep the descriptions concise.

	$D_{\parallel} \ll D_{\Omega}$	$D_{\parallel} \gg D_{\Omega}$
$D_{\perp} \gg D_{\Omega}$	NEUTRAL: idealized interfaces	ENHANCING: additional transport in GBs
$D_{\perp} \ll D_{\Omega}$	BLOCKING: hindered transport	CONNECTING: GB segments as channels

Table 1: Diffusion regimes to characterize the impact of GB transport on the overall system response.

4.3 Characterizing transport in GBs

Approaches that account for concentration jumps across GBs [40, 41] can recover the local flux of ions across the GB. For a Fisher-like model the in- and outflux of the GB was related to the in-plane gradient [37]. However, beyond that, the condensed representation of the GB in the Fisher-like model generally remains a severe limitation when investigating the local transport of ions within the GB. In this context, the three-node-collapsed analytical design of the proposed GB diffusion model from eq. (10) and eq. (19) is of particular importance and interest. It allows us to analyze the relevant modes of GB transport and enables the full reconstruction of the 3D GB volume and corresponding concentration profiles as discussed in the following.

The coefficients of the analytical GB profile in eq. (10)

$$\alpha_0(\mathbf{x}_{\parallel}) = c(\zeta_t, \zeta_n = 0), \quad (61)$$

$$\alpha_1(\mathbf{x}_{\parallel}) = \frac{1}{2} \left(c(\zeta_t, \zeta_n = h) - c(\zeta_t, \zeta_n = -h) \right), \quad (62)$$

$$\alpha_2(\mathbf{x}_{\parallel}) = \frac{1}{2} \left(c(\zeta_t, \zeta_n = h) - 2c(\zeta_t, \zeta_n = 0) + c(\zeta_t, \zeta_n = -h) \right) \quad (63)$$

determine the magnitude of the constant, linear and quadratic modes in the model. Hence, their distribution over the entire geometry can be used to characterize GB transport depending on the parameter configuration as shown in Figure 10. The first-order coefficient $\alpha_1(\mathbf{x}_{\parallel})$ is directly related to the concentration jump $\llbracket c \rrbracket$ via $2|\alpha_1(\mathbf{x}_{\parallel})| = \llbracket c \rrbracket = |c(\zeta_t, \zeta_n = h) - c(\zeta_t, \zeta_n = -h)|$. The second-order coefficient $\alpha_2(\mathbf{x}_{\parallel})$ appears in the net influx into the GB which we define as

$$q_{\text{in}}(\mathbf{x}_{\parallel}) = D_{\perp} \left(\left. \frac{\partial c(\zeta_t, \zeta_n)}{\partial \zeta_n} \right|_{\zeta_n=h} - \left. \frac{\partial c(\zeta_t, \zeta_n)}{\partial \zeta_n} \right|_{\zeta_n=-h} \right) \quad \text{with } q_{\text{in}} \begin{cases} > 0 : & \text{influx} \\ < 0 : & \text{outflux} \end{cases} \quad (64)$$

based on the normal fluxes on both sides of the GB. The quantities are directly related via $D_{\perp} \frac{4}{h} \alpha_2(\mathbf{x}_{\parallel}) = q_{\text{in}}(\mathbf{x}_{\parallel})$.

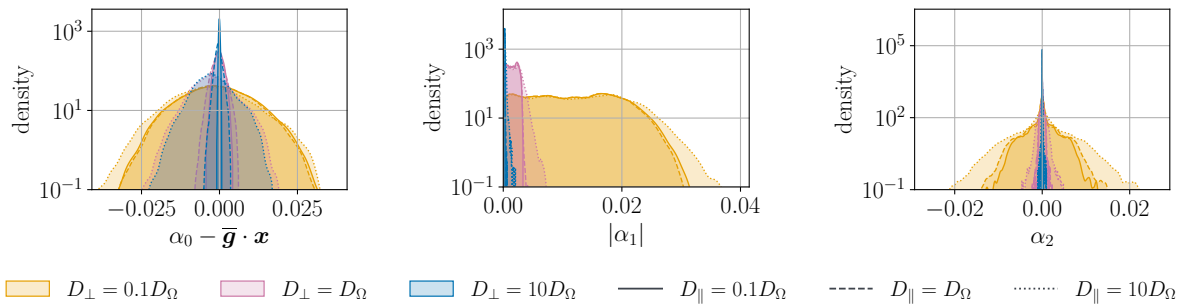


Figure 10: Geometry-wide distribution of element-averaged $\alpha_0 - \bar{\mathbf{g}} \cdot \mathbf{x}$ (fluctuation-based offset, cf. eq. (6)), α_1 (jump) and α_2 (channeling) in eq. (10) for different parameter configurations: The choice of D_{\perp}/D_{Ω} is indicated by the color whereas D_{\parallel}/D_{Ω} is determined by the linestyle. The GB thickness was fixed to be $h = 0.0032l$ ($f_{\text{GB}} \approx 7.80\%$) to match the results in Figure 11). The density profiles were computed using kernel density estimation on the element averages (independent of the element volumes). Note that this might introduce a slight bias depending on the variance in the element volumes, e.g., close to grain edges or vertices.

The reconstruction of the 3D GB volume is achieved by shifting the top and bottom node layer of a given collapsed interface outwards and inwards, respectively, by the GB thickness parameter h . In the following, an arbitrary grain within the geometry (highlighted in Figure 11) is used for an in-depth analysis. In Figure 11, the concentration field within the extruded GB volume is shown for the selected grain to underline the capabilities of this reconstruction approach.

In the following the interplay of Figure 10 and Figure 11 allows for detailed insights into the global relevance of the different modes as well as their dependence on local features such as interface orientation.

Starting from the limit case of the *neutral* regime the concentration jump across the GB, represented by $\alpha_1(\mathbf{x}_{\parallel})$, grows significantly for $D_{\perp} \ll D_{\Omega}$ as shown in Figure 10. Increasing D_{\perp}/D_{Ω} (that is, lowering the resistance) leads to negligible concentration jumps. This implies a strong dependence of the jump magnitude on the orientation of the interface with respect to the direction of the imposed gradient which can be verified in Figure 11 for the *connecting* regime³: Larger jumps are observed the more the normal vector aligns with the direction of the imposed gradient (i.e., the x -direction in the case of Figure 11). Due to the nearly isotropic structure of the geometry the distribution of $\alpha_1(\mathbf{x}_{\parallel})$ in Figure 10 is relatively uniform for $D_{\parallel} \ll D_{\Omega}$. However, for $D_{\parallel} \gg D_{\Omega}$ the enhanced transport along the GB leads to a stronger impact of the local geometry arrangement and smears out the distribution profile, leading to even larger jumps.

The second-order term $\alpha_2(\mathbf{x}_{\parallel})$ accounts for the channeling effect of ion transport along GBs. The distribution in Figure 10 shows a similar dependence on D_{\perp} as described for the case of α_1 : A larger resistance in normal direction ($D_{\perp} \ll D_{\Omega}$) enables the formation of a second-order profile. The range of $\alpha_2(\mathbf{x}_{\parallel})$ is additionally enhanced by increasing D_{\parallel}/D_{Ω} . Hence, the *connecting* regime exhibits the strongest channeling effects that we explicitly wanted to account for by Assumption [A5]. In alignment with the concentration jump, the second-order mode also depends on the orientation of the interface: In the displayed concentration profiles of Figure 11 a growing second-order mode can be observed as the GB plane aligns with the direction of the imposed gradient. This can be better understood when considering the α_2 -related net influx for the selected grain in the top right of Figure 11: It shows a net influx of ions on the left of the facets and an outflux on the right of the facets. A net outflux ($q_{\text{in}} < 0$) corresponds to an accumulation of ions at the middle plane whereas a net influx ($q_{\text{in}} > 0$) is the result of a local minimum of ions at the GB center. This induces enhanced transport along the GB middle plane from local maximum to local minimum which is consistent with the symmetric density profiles that were found for α_2 in Figure 10. The role of GB junctions with respect to the second-order modes should also be mentioned briefly: At any junction where different GB segments meet, the central node on the middle layer is shared among all segments. This approximation necessarily introduces artifacts along grain edges and corners that might alter the reconstructed profiles and modes. The extreme second-order modes close

³In fact the largest concentration jumps and second order coefficients can be observed within the *connecting* regime (see Figure 10) which was the motivation for the choice of this parameter configuration in Figure 11.

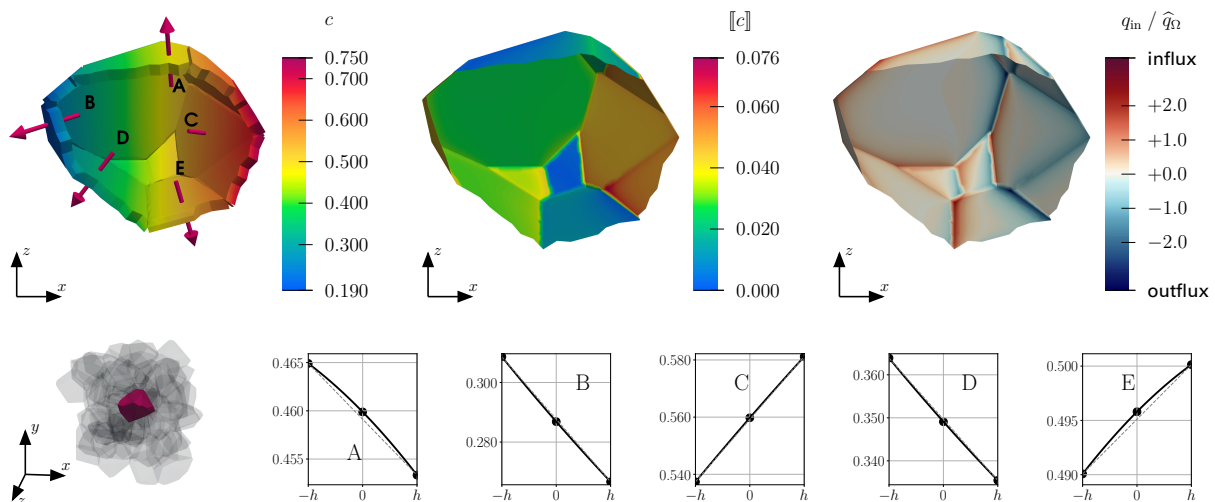


Figure 11: In-depth analysis of the GB domain for a selected grain (position in the geometry displayed at the bottom left) which is cut in half and a fixed parameter configuration ($D_{\parallel} = 10D_{\Omega}$, $D_{\perp} = 0.1D_{\Omega}$, $h = 0.0032l$, $f_{\text{GB}} \approx 7.80\%$). **Top left:** Reconstruction of the concentration profile. Note that the GB plane was extruded by a factor of $0.01l > h$ in this case to enhance the visibility of the discussed effects. For selected points, the concentration profile across the GB (in the direction of the respective arrow) is shown in the bottom row. The dashed lines are added to underline the effect of the second-order mode. **Top center:** Absolute concentration jump $[[c]]$ across the GB. **Top right:** Net influx into the GB as defined in eq. (64). The flux is dedimensionalized with $\hat{q}_{\Omega} = \|\mathbf{-D}_{\Omega}\bar{\mathbf{y}}\|$. The sign of q_{in} determines the flow direction as indicated.

to the junctions in Figure 11 are (partially) caused by this and lead to the rapid decay of the α_2 -density profiles in Figure 10 in the *connecting* regime.

To shed light on the interplay of the discussed GB transport mechanisms, the GB flux fields of the four limiting cases of the different regimes are compared. In Figure 12 3D fields are reconstructed in the same way as the concentration profiles in Figure 11. This enables direct insight into where ions enter, diffuse along, and exit the GB.

For the *neutral* (Figure 12a) and the *blocking* regime (Figure 12c) the flux aligns with the interface normal. Its magnitude exhibits a significant dependence on the respective facet orientation, as observed for the first mode in Figure 11, where the flux increases the more aligned facet normal and direction of the imposed gradient are. For the *blocking* regime, however, the magnitude of the flux is further altered by the local geometry arrangement.

Opposed to that, the increase in D_{\parallel}/D_{Ω} leads to more in-plane dominated transport in case of the *enhancing* (Figure 12b) and *connecting* regime (Figure 12d). Despite that, the characteristics of the two regimes still differ significantly. For the *enhancing* regime the flux magnitude increases if interfaces align with the direction of the imposed gradient, indicating that ions do not deviate significantly from the shortest diffusion paths in a global sense. This aligns with the properties of the second-order mode in Figure 11. At the same time the local geometry causes variance in magnitude within the individual facets.

Lastly, the channeling effect in the *connecting* regime as observed in the concentration profiles of Figure 11 is clearly visible in Figure 12d: An amplified in-plane flux within the middle layer of the GB can be observed that is impacted by the orientation of the GB segments. In the top and bottom layer of the GB, which are directly coupled with the bulk domain, flux happens in inverse direction. The channeling effect causes a suction effect that alters the transport behavior in the surrounding bulk domain. Hence, the transport within the grains itself is very limited, and the GB channels connect the individual grains, which only show little fluctuation from constant concentration levels. The significant local variations in the orientation of the in-plane flux hint at the strong impact of the local geometry arrangement.

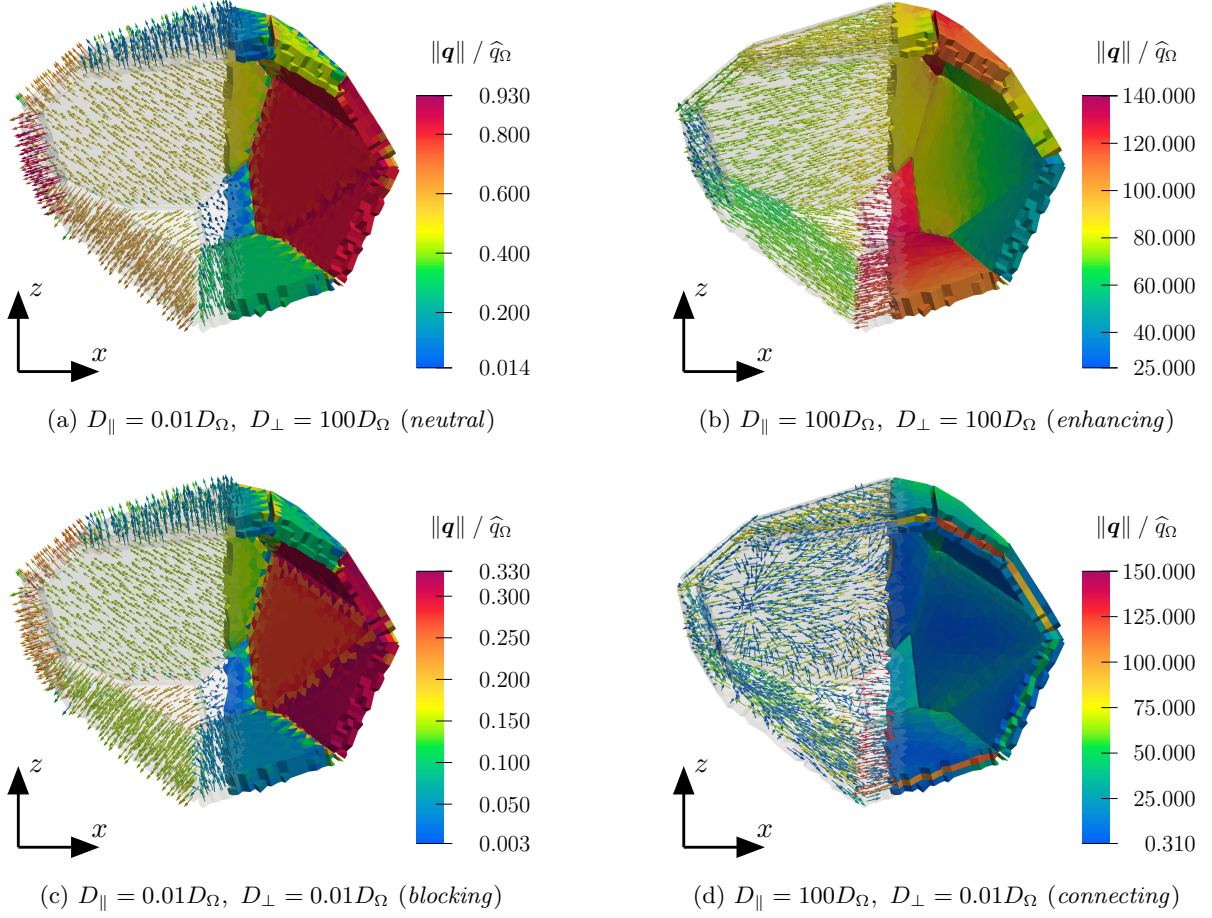


Figure 12: Dedimensionalized flux within the extruded GB of the selected grain introduced in Figure 11 for an imposed gradient \bar{g} in x -direction: The flux is dedimensionalized with $\hat{q}_{\Omega} = \|\bar{g}\|$. Magnitude as well as direction of the flux field are displayed for varying combinations of D_{\parallel}/D_{Ω} and D_{\perp}/D_{Ω} . In accordance with Figure 11 we set $h = 0.0032l$ such that $f_{\text{GB}} \approx 7.80\%$. However, the GB was extruded by $0.01l$ to show an enhanced GB effect.

4.4 Quantifying the impact of GB transport

In many applications, it is mainly the average behavior or effective diffusion tensor on the mesoscale resulting from a certain microscale geometry and parametrization that is of interest. Hence, the effect of parameter variations on the effective behavior is further investigated. The eigenvalues of the diffusion tensor $\underline{\underline{D}}$ for different slices of the parameter space are shown in Figure 13. The largest eigenvalue of the diffusion tensor is a suitable indicator for the behavior of the entire tensor due to the close-to isotropic structure of the considered geometry (cf. eq. (59)). For the *neutral* regime, the effective eigenvalue converges towards the bulk one. Opposed to that, the effective diffusion coefficients are maximized in the case of the *enhancing* regime due to the additional GB transport. It is further increased for a larger thickness parameter h of the GB and, therefore, larger volume fractions of the more conductive GB. This effect is clearly governed by $D_{\parallel} \gg D_{\Omega}$ since the *connecting* regime also exhibits a magnified eigenvalue, albeit to a lesser extent. Considering that D_{\perp} limits the ability to cross the GB, the effective eigenvalue is found to be decreased below D_{Ω} for the *blocking* regime. In summary, the effective diffusion behavior is mainly altered for $D_{\perp} \ll D_{\Omega}$ and/or $D_{\parallel} \gg D_{\Omega}$. This again stresses the importance of accounting for an anisotropic GB, i.e., for D_{\parallel} and D_{\perp} separately.

In general, the underlying anisotropy of the polycrystalline geometry affects the effective diffusion tensor in a structural and quantitative way. However, Figure 13 shows that the geometrical anisotropies have a varying impact within the different parametric regimes. For the bulk-like behavior in the *neutral* regime, the specific arrangement and orientation of the GB segments do not really play a role. In this case we

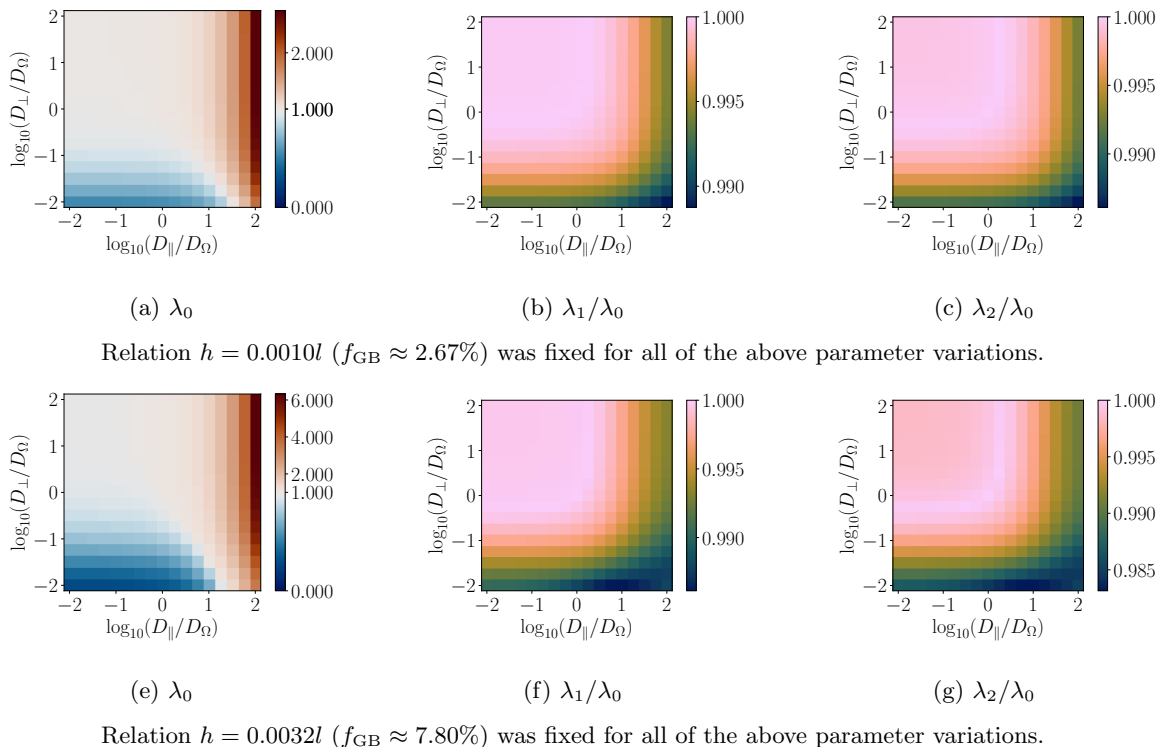


Figure 13: Eigenvalues λ_i of the dedimensionalized effective diffusivity tensor $\underline{\underline{D}}/D_\Omega$ for varying diffusion parameters in the GB. For comparability, the largest eigenvalue λ_0 and the ratios of λ_1 and λ_2 are given, respectively.

find $\lambda_0 \approx \lambda_1 \approx \lambda_2$.

As pointed out in Section 4.2, the diffusion behavior becomes less dependent on the GB segment orientation and more dependent on the local geometry arrangement for $D_\perp \ll D_\Omega$. This observation is underlined by the effective diffusion tensor showing the most pronounced anisotropy in the *blocking* and *connecting* regime. A similar but weaker effect can be seen for the *enhancing* regime. The use of GBs as preferred diffusion paths also stresses the dependence on geometry and anisotropic features.

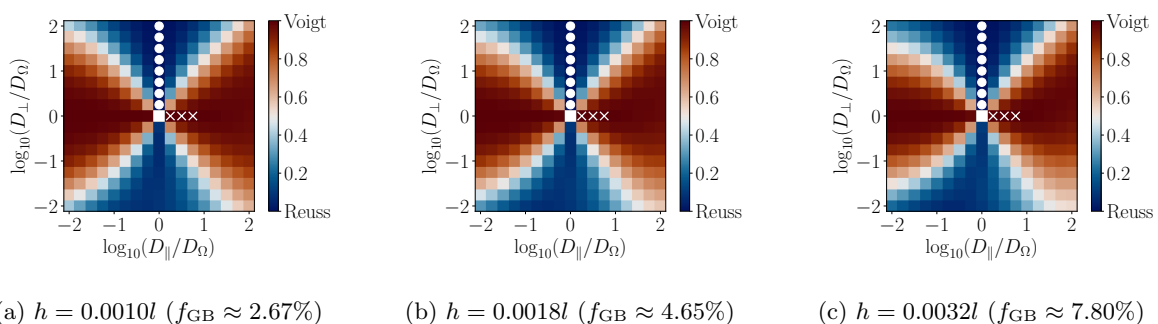


Figure 14: Relation of the effective diffusivity tensor to the analytical Voigt bound (value 1) and the Reuss bound (value 0). The computations follow the remarks in Section 2.4.3. Numerical violations of the bounds are marked with \circ for the Reuss bound and \times for the Voigt bound.

The relation of $\underline{\underline{D}}$ with respect to the analytical Voigt-Reuss bounds as derived in eq. (46) and eq. (47) is shown in Figure 14. The Voigt-Reuss relations for the given 3D polycrystal example show a great similarity with the 2D example (cf. Figure 6c): For extreme D_\parallel -configurations the solution is close to the Voigt bound while for extreme D_\perp -configurations it is close to the Reuss bound. This behavior stems from the observation mentioned above that D_\perp , in general, has a rather hindering impact on the overall diffusion behavior and, therefore, pushes the effective diffusion tensor closer to the lower bound. Opposed

to that, the additional transport that is enabled through in-plane diffusion along the GBs yields effective responses close to the upper bound. For an isotropic GB ($D_{\parallel} = D_{\perp}$), the effective diffusion coefficient is close to Hill's estimate [62], which is the arithmetic mean of the upper (Voigt) and lower (Reuss) bounds. Interestingly, a similar effect can be observed for $D_{\parallel}D_{\perp} = 1$. This implies that D_{\parallel} and D_{\perp} can balance out each other's effects in some sense.

As discussed for the 2D validation example, slight numerical violations of the bounds are obtained, as highlighted. However, their magnitude is of less than 0.1%, meaning in a similar range compared to the 2D example. Furthermore, the structure of the relation in the parameter space gradually loses its symmetry for increased volume fractions, i.e., larger values for h/l . One possible interpretation is the growing inapplicability of the proposed model and the compensation (see Section 2.4.2) for too-thick GBs. Note that the determination of a distinct limit value for the validity of the model, however, is non-trivial.

5 Application of the model under realistic conditions

We conclude the parametric analysis by consideration of a realistic setup for $\text{Li}_6\text{PS}_5\text{Cl}$: In our recent study [11], diffusion parameters for the bulk and three GB types were obtained by means of molecular dynamics simulations accelerated by machine-learning interatomic potentials. The temperature dependence of the structure-specific diffusion parameters is directly given via the Arrhenius relation as stated in eq. (7). The investigated GB types are either in the *enhancing* regime (for anion-ordered bulk) or in the *blocking* regime (for bulk with 50% Cl/S-anion disorder). For the sake of brevity, we consider the isotropic anion-ordered bulk together with the GB type $\Sigma 5(001)[001]$ here since it shows the most significant anisotropy among the GB types studied carefully in Ref. [11]. Parameters and further remarks on the setup are given in Appendix C.

The differences in the Arrhenius parameters for bulk and GB suggest a temperature-dependent non-Arrhenius behavior for a mixture of these, meaning a polycrystal, on mesoscale. With the proposed collapsed approach we are able to investigate and quantify this in detail and also outside of the temperature range that can be considered in atomistic simulations, including room temperature. The effective diffusion coefficient for the considered polycrystalline geometry as a function of temperature is shown in Figure 15. Two representative grain sizes have been chosen to show the size effect. Note that both choices satisfy $f_{\text{GB}} < 10\%$, i.e., the assumption of a clear length separation between grain size and GB thickness is reasonable.

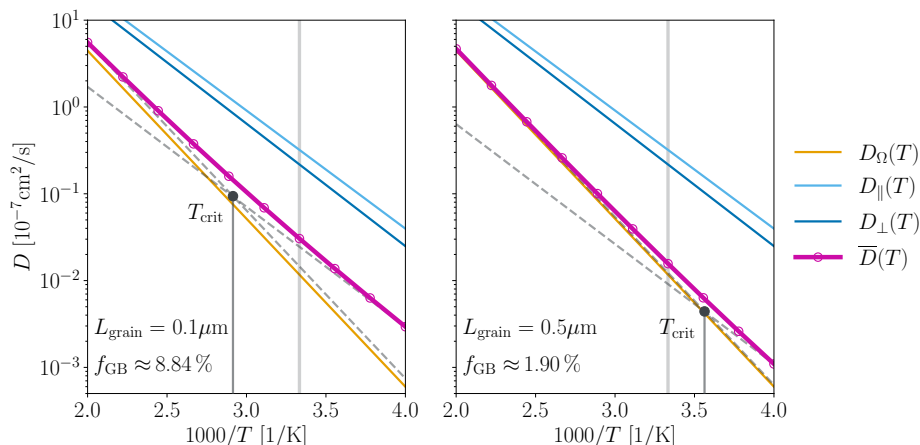


Figure 15: Temperature dependence of the largest eigenvalue of the effective diffusion tensor for two different average grain sizes L_{grain} with resulting volume fractions f_{GB} : The phase-specific parameters D_{Ω} , D_{\parallel} and D_{\perp} which follow the Arrhenius relation from eq. (7) are also shown. To underline the non-Arrhenius response of the polycrystal the critical temperature T_{crit} [16] (see Appendix C) is constructed (dashed lines). For reference, room temperature ($T = 300$ K) is marked by the gray vertical line.

For large temperatures, the effective response is strongly bulk-dominated. However, for small temperatures, the contrast between the bulk and GB properties becomes more significant, leading to a larger

GB impact on the effective properties. To underline the transition from the bulk- to the GB-dominated regime, we construct the critical temperature T_{crit} [16] (see Appendix C) which is highlighted in Figure 15. The critical temperature T_{crit} and, therefore, the regimes of bulk- and GB-dominated response clearly depend on the GB volume fraction. For larger volume fractions the relevance of the GB is increased. To conclude, the influence of the GB is clearly notable around the room temperature level even for reasonable volume fractions and should not be neglected.

In practice, however, the exact share of disorder in the bulk remains hard to control and determine. Furthermore, the assumption of identical properties in all GB segments does not hold. The effects of the latter have been partially studied in Ref. [40] by splitting the set of GB segments into subsets with uniform properties, which can lead to percolation paths.

6 Summary and conclusions

We have proposed a new collapsed interface finite element to account for transversely isotropic ion diffusion properties of grain boundaries (GBs) in polycrystalline materials. The theoretical considerations for a simple channel flow problem in Assumption [A5] as well as the symmetric 2D validation example in Section 3 underline the need to account for an approximation of at least second order when modeling the concentration field inside the GB. The resulting model captures concentration offsets, jumps, and channeling effects and can be collapsed, yielding zero-thickness interface elements due to its analytical description along the thickness direction. Thereby, an accurate representation of GB effects is enabled without fully resolving these thin interface layers within the bulk discretization. Furthermore, this allows for size as well as interface thickness effects to all be studied on the same mesh, which is highly advantageous in terms of computational cost. Exploitation of the affine parameter dependence of the problem drastically reduces the number of required simulations by moving from an initial 5D parameter space to a 2D domain. This could also be further exploited by a surrogate model as done for the effective response of simpler GB models (e.g., Ref. [40]) to replace overly simplified averages (e.g., Refs. [15, 17]).

In a postprocessing step the full GB domain and concentration profiles can be reconstructed for in-depth studies by exploiting the analytical description across the GB thickness. By doing so we overcome the limitations of previous FE approaches (e.g., Refs. [37, 40]) where only the bulk domain is investigated while the inside of the GB and corresponding mechanisms remain unexplored.

A significant impact of the GB properties on the overall diffusion behavior as well as on the effective properties was found which is reflected in four regimes as defined in Table 1: Starting from the case of idealized interfaces (*neutral* regime) the overall transport is severely limited if the GB conductivity in the normal direction is reduced (*blocking* regime). Then the GB hinders ions from crossing the GB region, effectively reducing trans-GB flow. Opposed to that, the conductivity along the GB plays an enhancing role with respect to the overall transport by allowing for additional diffusion paths along the GB (*enhancing* regime). This is also reflected by the streamlines deviating significantly from the shortest direct diffusion paths for some configurations, indicating that the ions prefer to take detours due to GB effects. In some cases, a pronounced ion channeling effect was observed (*connecting* regime). Accordingly, the effective diffusion coefficients are increased or reduced depending on the GB properties. All of the described effects are amplified for larger GB volume fractions, i.e., thicker GBs. Interestingly, the normal and the tangential part of the stiffness matrix and of the right hand side vector scale with $1/h$ and h , respectively (see eq. (54)). In addition, the effect on the effective flux is proportional to h . This highlights that changes in the GB width $2h$ can lead to nontrivial changes of the related flow field.

While the presented model focuses solely on Fickian diffusion, the model can also be extended to the consideration of electric driving forces without significant changes to its structure as discussed in Section 2.1. Furthermore, the presented work forms a solid foundation for further extensions towards more realistic polycrystalline setups. This might include:

- **Interplay of different GB types:** The parametrization of the model within this work can be extended to different GB types and anisotropic bulk behavior without additional effort or significant adaptations in the model. This enables the upscaling of realistic scenarios from atomistic to larger continuum scales given the availability of comprehensive atomistic data.

- **Sensitivity to geometrical features:** The present study has focused on the impact of material properties as well as the artificially introduced GB volume fraction. In practice, however, the local geometry arrangement introduces additional variability of the material response [40, 63].
- **Extension of the range of admissible volume fractions:** The collapsed interface model relies on the assumption of the GB thickness $2h$ being *small* with respect to the grain size L_{grain} . For regimes of larger volume fractions alternative approaches with potentially fully-resolved GBs need to be considered that could then be used to check the consistency within the transition region.

Overall, this study has underlined that the varying GB properties of different GB types and in the normal as well as tangential direction that were found on atomistic scale [11] can have a non-negligible relevance for diffusion on larger scales up to the engineering scale. By means of the proposed model, a clear and detailed understanding of the local transport mechanisms and the resulting overarching parametric regimes was gained in a computationally efficient manner. On the one hand, the provided forward model can yield accurate predictions. On the other hand, it can be used to solve inverse problems, e.g., to identify an admissible range of the degree of anion disorder based on a small number of experimental datasets, a quantity very hard to access from direct experiments.

Provided that data on bulk and GB properties is available from atomistic simulations, the presented findings also offer valuable knowledge about when GBs need to be modeled and when their impact is minimal enough to be overlooked. Beyond GBs, other interface diffusion processes such as transport along metal/ceramic interfaces were found to exhibit a GB-like behavior, see, e.g., Ref. [64]. Due to its general formulation the applicability of the proposed interface model can, therefore, be extended to other use cases.

CRediT authorship contribution statement

L. Scholz: Conceptualization, Methodology, Software, Visualization, Writing - Original draft **Y. Ou:** Conceptualization, Writing - Review and editing **B. Grabowski:** Funding acquisition, Conceptualization, Writing - Review and editing **F. Fritzen:** Funding acquisition, Conceptualization, Methodology, Writing - Original draft, Supervision

Declaration of competing interest

The authors declare that they have no conflict of interest.

Acknowledgement

This project is funded by the Deutsche Forschungsgemeinschaft (DFG, German Research Foundation) - EXC 2075 - 390740016 under Germany's Excellence Strategy (L. Scholz and Y. Ou); FR 2702/10 - 517847245 (F. Fritzen). B. Grabowski is funded by the European Research Council (ERC) under the European Union's Horizon 2020 Research and Innovation Program (Grant Agreement No. 865855). The authors acknowledge the support by the Stuttgart Center for Simulation Science (SimTech).

Data availability

The simulation results for the homogenized responses across the parameter space will be published on DaRUS, the data repository of the University of Stuttgart, upon acceptance.

Appendix

A Finite element (FE) discretization

A.1 3D bulk domain

Within the bulk we use classical Lagrange elements with quadratic shape functions, that is, a ten node tetrahedron as depicted in fig. 16a. In the reference coordinates $\underline{\eta} = [\eta_1, \eta_2, \eta_3]$, the shape functions are

$$\underline{N}_\Omega(\underline{\eta}) = \begin{bmatrix} (2(1 - \eta_1 - \eta_2 - \eta_3) - 1)(1 - \eta_1 - \eta_2 - \eta_3) \\ (2\eta_1 - 1)\eta_1 \\ (2\eta_2 - 1)\eta_2 \\ (2\eta_3 - 1)\eta_3 \\ 4(1 - \eta_1 - \eta_2 - \eta_3)\eta_1 \\ 4\eta_1\eta_2 \\ 4(1 - \eta_1 - \eta_2 - \eta_3)\eta_2 \\ 4(1 - \eta_1 - \eta_2 - \eta_3)\eta_3 \\ 4\eta_1\eta_3 \\ 4\eta_2\eta_3 \end{bmatrix}^\top \in \mathbb{R}^{1 \times 10}. \quad (\text{A1})$$

The corresponding gradient with respect to the reference coordinates is

$$\underline{B}_\Omega^{\text{ref}}(\underline{\eta}) = \begin{bmatrix} 4(\eta_1 + \eta_2 + \eta_3) - 3 & 4(\eta_1 + \eta_2 + \eta_3) - 3 & 4(\eta_1 + \eta_2 + \eta_3) - 3 \\ 4\eta_1 - 1 & 0 & 0 \\ 0 & 4\eta_2 - 1 & 0 \\ 0 & 0 & 4\eta_3 - 1 \\ -4(2\eta_1 + \eta_2 + \eta_3 - 1) & -4\eta_2 & -4\eta_3 \\ 4\eta_2 & 4\eta_1 & 0 \\ -4\eta_1 & -4(2\eta_1 + \eta_2 + \eta_3 - 1) & -4\eta_3 \\ -4\eta_1 & -4\eta_2 & -4(2\eta_1 + \eta_2 + \eta_3 - 1) \\ 4\eta_3 & 0 & 4\eta_1 \\ 0 & 4\eta_3 & 4\eta_2 \end{bmatrix}^\top \in \mathbb{R}^{3 \times 10}. \quad (\text{A2})$$

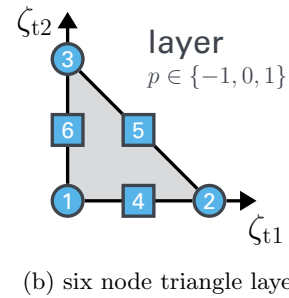
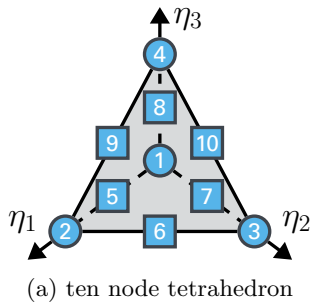


Figure 16: Reference elements for the FE discretization.

A.2 2D grain boundary interface domain

The proposed interface elements are described within the reference coordinates $\underline{\zeta} = [\zeta_{t1}, \zeta_{t2}, \zeta_n]$ where $\underline{\zeta}_t = [\zeta_{t1}, \zeta_{t2}]$ form the interface plane and ζ_n represents the interface normal of the prism element (see Section 2.3.2). On the surface, only the $\underline{\zeta}_t$ coordinates of the reference element are used to define the

6-node triangular element, as shown in fig. 16b. The corresponding shape functions are defined as:

$$\underline{N}_{\text{P2}}(\underline{\zeta}_t) = \begin{bmatrix} (1 - \zeta_{t1} - \zeta_{t2})(1 - 2\zeta_{t1} - 2\zeta_{t2}) \\ \zeta_{t1}(2\zeta_{t1} - 1) \\ \zeta_{t2}(2\zeta_{t2} - 1) \\ 4\zeta_{t1}(1 - \zeta_{t1} - \zeta_{t2}) \\ 4\zeta_{t1}\zeta_{t2} \\ 4\zeta_{t2}(1 - \zeta_{t1} - \zeta_{t2}) \end{bmatrix}^T \in \mathbb{R}^{1 \times 6}. \quad (\text{A3})$$

The gradient with respect to the reference coordinates then is

$$\underline{B}_{\text{P2}}^{\text{ref}}(\underline{\zeta}_t) = \begin{bmatrix} -3 + 4(\zeta_{t1} + \zeta_{t2}) & -3 + 4(\zeta_{t1} + \zeta_{t2}) \\ -1 + 4\zeta_{t1} & 0 \\ 0 & -1 + 4\zeta_{t2} \\ 4(1 - 2\zeta_{t1} - \zeta_{t2}) & -4\zeta_{t1} \\ 4\zeta_{t2} & 4\zeta_{t1} \\ -4\zeta_{t2} & 4(1 - \zeta_{t1} - 2\zeta_{t2}) \end{bmatrix}^T \in \mathbb{R}^{2 \times 6}. \quad (\text{A4})$$

Note that this gradient is defined on a 2D submanifold and needs to be transformed to the 3D space as described in Section 2.3.2.

B Affine parameter dependence

In the following a more detailed derivation of the affine dependencies for the parameter set given in eq. (52) is provided with respect to the reference quantities D_0 for the diffusion coefficients and l_0 for the geometry scaling. The superscript 0 is used to indicate that the respective quantity depends on the reference quantities D_0 and l_0 alone and not on the characteristic values.

B.1 Bulk domain

For the volume elements in the bulk domain, as introduced in Section 2.3.1, the integration weights ω_j and the gradient operator \underline{B}_{Ω} for a given element exhibit the following dependence:

$$\omega_j = \pi_l^3 \omega_j^0(l_0), \quad \underline{B}_{\Omega} = \left((\underline{B}_{\Omega}^{\text{ref}} \pi_l \underline{X}_{\Omega}^0(l_0)) \right)^{-1} \underline{B}_{\Omega}^{\text{ref}} = \frac{1}{\pi_l} \underline{B}_{\Omega}^0(l_0). \quad (\text{B1})$$

The element stiffness matrix \underline{K}_{Ω}^e (cf. eq. (15)) exhibits a dependence on π_{Ω} and π_l

$$\underline{K}_{\Omega}^e = \pi_{\Omega} D_0 \sum_{j=1}^{n_{\text{GP}}^{\Omega}} \pi_l^3 \omega_j^0(l_0) \frac{1}{\pi_l} \left(\underline{B}_{\Omega}^0(\underline{\eta}_j, l_0) \right)^T \frac{1}{\pi_l} \underline{B}_{\Omega}^0(\underline{\eta}_j, l_0) = \pi_{\Omega} \pi_l \underline{K}_{\Omega}^{e,0}(D_0, l_0) \quad (\text{B2})$$

where $\underline{K}_{\Omega}^{e,0}$ is independent of the characteristic values.

B.1.1 GB domain

The surface area of the individual interfaces scales according to

$$A_i = \pi_l^2 A_i^0(l_0). \quad (\text{B3})$$

The in-plane FE discretization using second-order triangles yields a dependence on π_l for the integration weights, shape functions and their gradient operator:

$$\nu_j = \pi_l^2 \nu_j^0(l_0), \quad \underline{N}_{\text{P2}} = \underline{N}_{\text{P2}}^0, \quad \underline{B}_{\text{P2}} = \frac{1}{\pi_l} \underline{B}_{\text{P2}}^0(l_0). \quad (\text{B4})$$

A dependence on the characteristic quantity accounting for the GB thickness is introduced via the analytical integration of the GB thickness for the stiffness matrices (cf. eq. (26) and eq. (27)):

$$\underline{\underline{K}}_{\parallel}^e = \frac{\pi_{\parallel} D_0 \pi_h l_0}{15} \begin{bmatrix} 4[*] & 2[*] & -[*] \\ 2[*] & 16[*] & 2[*] \\ -[*] & 2[*] & 4[*] \end{bmatrix} = \pi_{\parallel} \pi_h \underline{\underline{K}}_{\parallel}^{e,0}(D_0, l_0) \quad (\text{B5})$$

$$\underline{\underline{K}}_{\perp}^e = \frac{\pi_{\perp} D_0}{6\pi_h l_0} \begin{bmatrix} 7[**] & -8[**] & [**] \\ -8[**] & 16[**] & -8[**] \\ [**] & -8[**] & 7[**] \end{bmatrix} = \frac{\pi_{\perp} \pi_l^2}{\pi_h} \underline{\underline{K}}_{\perp}^{e,0}(D_0, l_0) \quad (\text{B6})$$

with

$$[*] = \sum_{j=1}^{n_{\text{GP}}^{\text{C18}}} \pi_l^2 \nu_j^0(l_0) \frac{1}{\pi_l} \left(\underline{\underline{B}}_{\text{P2}}^0(\zeta_{t(j)}, l_0) \right)^{\text{T}} \frac{1}{\pi_l} \underline{\underline{B}}_{\text{P2}}^0(\zeta_{t(j)}, l_0), \quad (\text{B7})$$

$$[**] = \sum_{j=1}^{n_{\text{GP}}^{\text{C18}}} \pi_l^2 \nu_j^0(l_0) \left(\underline{\underline{N}}_{\text{P2}}^0(\zeta_{t(j)}) \right)^{\text{T}} \underline{\underline{N}}_{\text{P2}}^0(\zeta_{t(j)}). \quad (\text{B8})$$

This yields the global system as stated in eq. (55) which depends on the two intrinsic parameters Π_{\parallel} and Π_{\perp} .

B.2 Effective properties and analytical bounds

The operators for integrating the gradient field over the respective domains $\mathbb{G}_{[\cdot]}$ (cf. eq. (39)-(41)) follow a scaling with π_h and π_l :

$$\mathbb{G}_{\Omega} = \sum_{i=1}^{n_{\text{el}}^{\Omega}} \sum_{j=1}^{n_{\text{GP}}^{\text{T10}}} \pi_l^3 \omega_j^0(l_0) \frac{1}{\pi_l} \underline{\underline{B}}_{\Omega}^0(\eta_j, l_0) \underline{\underline{L}}_{\Omega} = \pi_l^2 \mathbb{G}_{\Omega}^0(l_0), \quad (\text{B9})$$

$$\begin{aligned} \mathbb{G}_{\parallel} &= \frac{2\pi_h l_0}{6} \sum_{i=1}^{n_{\text{el}}^{\text{GB}}} \sum_{j=1}^{n_{\text{GP}}^{\text{C18}}} \pi_l^2 \nu_j^0(l_0) \frac{1}{\pi_l} \left[\underline{\underline{B}}_{\text{P2}}^0(\zeta_{t(j)}, l_0) \quad 4\underline{\underline{B}}_{\text{P2}}^0(\zeta_{t(j)}, l_0) \quad \underline{\underline{B}}_{\text{P2}}^0(\zeta_{t(j)}, l_0) \right] \underline{\underline{L}}_{\text{GB}} \\ &= \pi_h \pi_l \mathbb{G}_{\parallel}^0(l_0), \end{aligned} \quad (\text{B10})$$

$$\mathbb{G}_{\perp} = \sum_{i=1}^{n_{\text{el}}^{\text{GB}}} \sum_{j=1}^{n_{\text{GP}}^{\text{C18}}} \pi_l^2 \nu_j^0(l_0) \underline{\underline{n}}_i^0 \left[-\underline{\underline{N}}_{\text{P2}}^0(\zeta_{t(j)}) \quad \underline{\underline{0}} \quad \underline{\underline{N}}_{\text{P2}}^0(\zeta_{t(j)}) \right] \underline{\underline{L}}_{\text{GB}} = \pi_l^2 \mathbb{G}_{\perp}^0. \quad (\text{B11})$$

This yields the following dependencies for the phase-wise gradient averages (cf. eq. (38)):

$$\langle \underline{\underline{g}}_k \rangle_{\Omega} = \frac{1}{\pi_l} \underline{\underline{g}}_k + \frac{1}{\pi_l v_{\Omega}^0(l_0)} \mathbb{G}_{\Omega}^0 \tilde{\underline{\underline{c}}}_k, \quad (\text{B12})$$

$$\langle \underline{\underline{g}}_k \rangle_{\parallel} = \frac{1}{\pi_l} (\underline{\underline{I}} - \underline{\underline{S}}_{\perp}) \underline{\underline{g}}_k + \frac{1}{\pi_l 2l_0 A^0} \mathbb{G}_{\parallel}^0 \tilde{\underline{\underline{c}}}_k, \quad \langle \underline{\underline{g}}_k \rangle_{\perp} = \frac{1}{\pi_h 2l_0 A^0} \mathbb{G}_{\perp}^0 \tilde{\underline{\underline{c}}}_k. \quad (\text{B13})$$

The volumes of bulk v_{Ω} and GB domain v_{GB} scale with

$$v_{\Omega} = \pi_l^3 v_{\Omega}^0(l_0), \quad v_{\text{GB}} = \pi_h \pi_l^2 v_{\text{GB}}^0(l_0) \quad (\text{B14})$$

yielding the volume fractions (eq. (33)) to be given as

$$f_{\Omega} = \frac{v_{\Omega}^0(l_0)}{v_{\Omega}^0(l_0) + \frac{\pi_h}{\pi_l} v_{\text{GB}}^0(l_0)}, \quad f_{\text{GB}} = \frac{v_{\text{GB}}^0(l_0)}{\frac{\pi_l}{\pi_h} v_{\Omega}^0(l_0) + v_{\text{GB}}^0(l_0)}. \quad (\text{B15})$$

Since 5D parameter configurations $[\pi_{\Omega}, \pi_{\parallel}, \pi_{\perp}, \pi_h, \pi_l]$ mapping to one 2D configuration $[\Pi_{\parallel}, \Pi_{\perp}]$ yield identical fluctuation fields due to the lower intrinsic dimensionality, the parameter-free operators $\mathbb{G}_{[\cdot]}^0$ are identical as well and only need to be computed once for the entire set. However, the effective diffusion tensor (cf. eq. (45), that depends on the volume fractions (cf. eq. (33)), the volume-averaged

gradients and the individual diffusion coefficients via the fluxes (cf. eq. (44)), exhibits a dependence on the absolute values of the individual characteristic quantities. Hence, related 5D configurations yield the same fluctuation field but differing effective diffusion tensors.

The same holds for the analytical Voigt (eq. (46)) and Reuss bounds (eq. (47)):

$$\underline{\underline{D}}_V = D_0 \left(f_\Omega(\pi_h, \pi_l) \pi_\Omega \underline{\underline{I}} + f_{\text{GB}}(\pi_h, \pi_l) \pi_\parallel \left(\frac{\pi_\perp - \pi_\parallel}{\pi_\parallel} \underline{\underline{S}}_2^0 + \underline{\underline{I}} \right) \right), \quad (\text{B16})$$

$$\underline{\underline{D}}_R = D_0 \left(\frac{f_\Omega(\pi_h, \pi_l)}{\pi_\Omega} \underline{\underline{I}} + \frac{f_{\text{GB}}(\pi_h, \pi_l)}{\pi_\parallel} \left(\frac{\pi_\parallel - \pi_\perp}{\pi_\perp} \underline{\underline{S}}_2^0 + \underline{\underline{I}} \right) \right)^{-1}. \quad (\text{B17})$$

Note that the interface normals \underline{n}_i as well as the structural tensor $\underline{\underline{S}}_2 = \underline{\underline{S}}_2^0$ (cf. eq. (34)) are independent of the uniform scaling.

C Realistic setup for $\text{Li}_6\text{PS}_5\text{Cl}$

C.1 Translation of parameters

Ou et al. [11] obtained the fitted parameters D_0 and the activation energies E_a for bulk and different GB types from an Arrhenius fit. Together with the GB thickness the values are given in Table 2 for reference. For a given temperature T the diffusion coefficients D_Ω , D_\parallel and D_\perp (and their dedimensionalized

	D_0 [$10^{-7}\text{cm}^2/\text{s}$]	E_a [meV]	δ [\AA]
anion-ordered bulk	3.3×10^4	384	-
GB $\Sigma 5(001)[001]$ (\parallel)	1.1×10^4	270	26.5
GB $\Sigma 5(001)[001]$ (\perp)	1.1×10^4	280	

Table 2: Overview of parameters for $\text{Li}_6\text{PS}_5\text{Cl}$ as obtained by Ou et al. [11]: The parameters were fitted to simulation results in a temperature range from 500 to 800 K.

equivalents $\pi_\Omega, \pi_\parallel, \pi_\perp$) can be recovered from these values via the Arrhenius relation in eq. (7).

In the proposed model, the GB volume fraction is represented implicitly by scaling the GB thickness and geometric sample size via the dimensionless parameters π_h and π_l . Estimates for the actual GB thickness $\delta = 2h$ have been determined [11] (cf. Table 2) and therefore define π_h . For π_l , a more application-based perspective is used: Given the average grain volume $v_{\text{grain}} = v_\Omega/N$ we define the average grain size L_{grain} as the diameter of the sphere of volume v_{grain} :

$$L_{\text{grain}} := 2 \left(\frac{v_{\text{grain}}}{\frac{4}{3}\pi} \right)^{1/3} = 2\pi_l \left(\frac{v_{\text{grain}}^0}{\frac{4}{3}\pi} \right)^{1/3}. \quad (\text{C1})$$

By prescribing a realistic average grain size L_{grain} the parameter π_l is defined.

C.2 Non-Arrhenius behavior and critical temperature

In order to formalize the description of the non-Arrhenius behavior of the polycrystalline structure we make use of the critical temperature T_{crit} used by Heo et al.⁴ [16]. It denotes the transition temperature at which the effective diffusion coefficient switches from a bulk- to a GB-dominated behavior. For the construction of T_{crit} the intersection point of the tangents to the \overline{D} -curve in the Arrhenius plot is determined. Note that in the limit case of extreme temperatures the tangents correspond to the shifted lines of D_Ω and D_\parallel or D_\perp . For simplicity and in consistency with Heo. et al. we use the average of the GB diffusion coefficients $D_{\text{GB}}(T) := (D_\parallel(T) + D_\perp(T))/2$ for the construction. The construction is visualized in Figure 15 by means of the dashed lines.

⁴Note that Heo et al. used T_c when referring to the critical temperature. To avoid ambiguity with the concentration c , we chose to use T_{crit} in the following.

References

- [1] Y. Horowitz et al. “Between Liquid and All Solid: A Prospect on Electrolyte Future in Lithium-Ion Batteries for Electric Vehicles”. In: *Energy Technol.* 8.11 (2020), p. 2000580. DOI: 10.1002/ente.202000580.
- [2] T. Inoue and K. Mukai. “Are All-Solid-State Lithium-Ion Batteries Really Safe?—Verification by Differential Scanning Calorimetry with an All-Inclusive Microcell”. In: *ACS Appl. Mater. Interfaces* 9.2 (Jan. 2017), pp. 1507–1515. DOI: 10.1021/acsami.6b13224.
- [3] Y.-G. Lee et al. “High-Energy Long-Cycling All-Solid-State Lithium Metal Batteries Enabled by Silver–Carbon Composite Anodes”. In: *Nat. Energy* 5.4 (Apr. 2020), pp. 299–308. DOI: 10.1038/s41560-020-0575-z.
- [4] J. Sung, J. Heo, D.-H. Kim, S. Jo, Y.-C. Ha, D. Kim, S. Ahn, and J.-W. Park. “Recent Advances in All-Solid-State Batteries for Commercialization”. In: *Mater. Chem. Front.* 8.8 (2024), pp. 1861–1887. DOI: 10.1039/D3QM01171B.
- [5] K. J. Kim, M. Balaish, M. Wadaguchi, L. Kong, and J. L. M. Rupp. “Solid-State Li–Metal Batteries: Challenges and Horizons of Oxide and Sulfide Solid Electrolytes and Their Interfaces”. In: *Adv. Energy Mater.* 11.1 (2021), p. 2002689. DOI: 10.1002/aenm.202002689.
- [6] J.-S. Park, C.-H. Jo, and S.-T. Myung. “Comprehensive Understanding on Lithium Argyrodite Electrolytes for Stable and Safe All-Solid-State Lithium Batteries”. In: *Energy Storage Mater.* 61 (Aug. 2023), p. 102869. DOI: 10.1016/j.ensm.2023.102869.
- [7] M. Kim, J. Seo, J. P. D. Suba, and K. Y. Cho. “A Review of Polymers in Sulfide-Based Hybrid Solid-State Electrolytes for All-Solid-State Lithium Batteries”. In: *Mater. Chem. Front.* 7.22 (Nov. 2023), pp. 5475–5499. DOI: 10.1039/D3QM00729D.
- [8] Y. Chen and C. A. Schuh. “Geometric Considerations for Diffusion in Polycrystalline Solids”. In: *J. Appl. Phys.* 101.6 (Mar. 2007), p. 063524. DOI: 10.1063/1.2711820.
- [9] K. Jun, Y. Chen, G. Wei, X. Yang, and G. Ceder. “Diffusion Mechanisms of Fast Lithium-Ion Conductors”. In: *Nat. Rev. Mater.* 9.12 (Dec. 2024), pp. 887–905. DOI: 10.1038/s41578-024-00715-9.
- [10] M. Sadowski and K. Albe. “Grain Boundary Transport in the Argyrodite-Type Li₆PS₅Br Solid Electrolyte: Influence of Misorientation and Anion Disorder on Li Ion Mobility”. In: *Adv. Mater. Interfaces* 11.33 (2024), p. 2400423. DOI: 10.1002/admi.202400423.
- [11] Y. Ou, Y. Ikeda, L. Scholz, S. Divinski, F. Fritzen, and B. Grabowski. “Atomistic Modeling of Bulk and Grain Boundary Diffusion in Solid Electrolyte Li₆PS₅Cl Using Machine-Learning Interatomic Potentials”. In: *Phys. Rev. Mater.* 8.11 (Nov. 2024), p. 115407. DOI: 10.1103/PhysRevMaterials.8.115407.
- [12] R. Schlenker, A.-L. Hansen, A. Senyshyn, T. Zinkevich, M. Knapp, T. Hupfer, H. Ehrenberg, and S. Indris. “Structure and Diffusion Pathways in Li₆PS₅Cl Argyrodite from Neutron Diffraction, Pair-Distribution Function Analysis, and NMR”. In: *Chem. Mater.* 32.19 (Oct. 2020), pp. 8420–8430. DOI: 10.1021/acs.chemmater.0c02418.
- [13] J. A. Dawson, P. Canepa, M. J. Clarke, T. Famprakis, D. Ghosh, and M. S. Islam. “Toward Understanding the Different Influences of Grain Boundaries on Ion Transport in Sulfide and Oxide Solid Electrolytes”. In: *Chem. Mater.* 31.14 (July 2019), pp. 5296–5304. DOI: 10.1021/acs.chemmater.9b01794.
- [14] J. A. Dawson and M. S. Islam. “A Nanoscale Design Approach for Enhancing the Li-Ion Conductivity of the Li₁₀GeP₂S₁₂ Solid Electrolyte”. In: *ACS Mater. Lett.* 4.2 (Feb. 2022), pp. 424–431. DOI: 10.1021/acsmaterialslett.1c00766.
- [15] J. S. Yoon, H. Sulaimon, and D. J. Siegel. “Exploiting Grain Boundary Diffusion to Minimize Dendrite Formation in Lithium Metal-Solid State Batteries”. In: *J. Mater. Chem. A* 11.43 (Nov. 2023), pp. 23288–23299. DOI: 10.1039/D3TA03814A.

- [16] T. W. Heo et al. “Microstructural Impacts on Ionic Conductivity of Oxide Solid Electrolytes from a Combined Atomistic-Mesoscale Approach”. In: *npj Comput. Mater.* 7.1 (Dec. 2021), pp. 1–15. DOI: 10.1038/s41524-021-00681-8.
- [17] J. A. Dawson, P. Canepa, T. Famprakis, C. Masquelier, and M. S. Islam. “Atomic-Scale Influence of Grain Boundaries on Li-Ion Conduction in Solid Electrolytes for All-Solid-State Batteries”. In: *J. Am. Chem. Soc.* 140.1 (Jan. 2018), pp. 362–368. DOI: 10.1021/jacs.7b10593.
- [18] A. V. Shapeev. “Moment Tensor Potentials: A Class of Systematically Improvable Interatomic Potentials”. In: *Multiscale Model. Simul.* 14.3 (Jan. 2016), pp. 1153–1173. DOI: 10.1137/15M1054183.
- [19] E. Milan and M. Pasta. “The Role of Grain Boundaries in Solid-State Li-metal Batteries”. In: *Mater. Futures* 2.1 (Dec. 2022), p. 013501. DOI: 10.1088/2752-5724/aca703.
- [20] E. W. Hart. “On the Role of Dislocations in Bulk Diffusion”. In: *Acta Metall.* 5.10 (Oct. 1957), p. 597. DOI: 10.1016/0001-6160(57)90127-X.
- [21] J. C. M. Garnett and J. Larmor. “XII. Colours in Metal Glasses and in Metallic Films”. In: *Philos. Trans. R. Soc. A* 203.359-371 (Jan. 1904), pp. 385–420. DOI: 10.1098/rsta.1904.0024.
- [22] I. V. Belova and G. E. Murch. “Diffusion in Nanocrystalline Materials”. In: *J. Phys. Chem. Solids* 64.5 (May 2003), pp. 873–878. DOI: 10.1016/S0022-3697(02)00421-3.
- [23] O. Wiener. “Die Theorie Des Mischkörpers Für Das Feld Der Stationären Strömung 1 Die Mittelwertsätze Für Kraft, Polarisaton Und Energie / von Otto Wiener”. In: *Abh. Königl. Sächs. Ges. Wiss.; 61,6* (1912).
- [24] W. Voigt. “Ueber Die Beziehung Zwischen Den Beiden Elasticitätsconstanten Isotroper Körper”. In: *Ann. Phys.* 274.12 (1889), pp. 573–587. DOI: 10.1002/andp.18892741206.
- [25] A. Reuss. “Berechnung Der Fließgrenze von Mischkristallen Auf Grund Der Plastizitätsbedingung Für Einkristalle .” In: *ZAMM - J. Appl. Math. Mech.* 9.1 (1929), pp. 49–58. DOI: 10.1002/zamm.19290090104.
- [26] T. Kanit, S. Forest, I. Galliet, V. Mounoury, and D. Jeulin. “Determination of the Size of the Representative Volume Element for Random Composites: Statistical and Numerical Approach”. In: *Int. J. Solids Struct.* 40.13 (June 2003), pp. 3647–3679. DOI: 10.1016/S0020-7683(03)00143-4.
- [27] D. Gryaznov, J. Fleig, and J. Maier. “Finite Element Simulation of Diffusion into Polycrystalline Materials”. In: *Solid State Sci. Solid State Reactivity - From Micro to Nano in Honour of Prof.Dr.h.c.Hermann Schmalzried on the Occasion of His 75th Birthday and the 99th Bunsen Colloquium* 10.6 (June 2008), pp. 754–760. DOI: 10.1016/j.solidstatesciences.2008.03.030.
- [28] M. V. Chepak-Gizbrekht and A. G. Knyazeva. “Grain-Boundary Diffusion Modeling in a Microstructural Material”. In: *Comput. Mater. Sci.* 184 (Nov. 2020), p. 109896. DOI: 10.1016/j.commatsci.2020.109896.
- [29] C. P. Schmidt, S. Sinzig, V. Gravemeier, and W. A. Wall. “A Three-Dimensional Finite Element Formulation Coupling Electrochemistry and Solid Mechanics on Resolved Microstructures of All-Solid-State Lithium-Ion Batteries”. In: *Comput. Methods Appl. Mech. Eng.* 417 (Dec. 2023), p. 116468. DOI: 10.1016/j.cma.2023.116468.
- [30] N. Pollmann, F. Larsson, K. Runesson, K. Lundgren, K. Zandi, and R. Jänicke. “Modeling and Computational Homogenization of Chloride Diffusion in Three-Phase Meso-Scale Concrete”. In: *Constr. Build. Mater.* 271 (Feb. 2021), p. 121558. DOI: 10.1016/j.conbuildmat.2020.121558.
- [31] M. Paggi and P. Wriggers. “A Nonlocal Cohesive Zone Model for Finite Thickness Interfaces – Part I: Mathematical Formulation and Validation with Molecular Dynamics”. In: *Comput. Mater. Sci.* 50.5 (Mar. 2011), pp. 1625–1633. DOI: 10.1016/j.commatsci.2010.12.024.
- [32] M. Paggi and P. Wriggers. “A Nonlocal Cohesive Zone Model for Finite Thickness Interfaces – Part II: FE Implementation and Application to Polycrystalline Materials”. In: *Comput. Mater. Sci.* 50.5 (Mar. 2011), pp. 1634–1643. DOI: 10.1016/j.commatsci.2010.12.021.

- [33] S. Firooz, P. Steinmann, and A. Javili. “Homogenization of Composites With Extended General Interfaces: Comprehensive Review and Unified Modeling”. In: *Appl. Mech. Rev.* 73.040802 (Aug. 2021). DOI: 10.1115/1.4051481.
- [34] S. Sinzig, C. P. Schmidt, and W. A. Wall. “A Conservative and Efficient Model for Grain Boundaries of Solid Electrolytes in a Continuum Model for Solid-State Batteries”. In: *J. Electrochem. Soc.* 171.4 (Apr. 2024), p. 040505. DOI: 10.1149/1945-7111/ad36e4.
- [35] J. C. Fisher. “Calculation of Diffusion Penetration Curves for Surface and Grain Boundary Diffusion”. In: *J. Appl. Phys.* 22.1 (Jan. 1951), pp. 74–77. DOI: 10.1063/1.1699825.
- [36] G. B. Gibbs. “Grain Boundary Impurity Diffusion”. In: *Phy. Status Solidi B* 16.1 (1966), K27–K29. DOI: 10.1002/pssb.19660160143.
- [37] S. Han, J. Park, W. Lu, and A. M. Sastry. “Numerical Study of Grain Boundary Effect on Li+ Effective Diffusivity and Intercalation-Induced Stresses in Li-ion Battery Active Materials”. In: *J. Power Sources* 240 (Oct. 2013), pp. 155–167. DOI: 10.1016/j.jpowsour.2013.03.135.
- [38] V. Lacaille, C. Morel, E. Feulvarch, G. Kermouche, and J. -. Bergheau. “Finite Element Analysis of the Grain Size Effect on Diffusion in Polycrystalline Materials”. In: *Comput. Mater. Sci.* 95 (Dec. 2014), pp. 187–191. DOI: 10.1016/j.commatsci.2014.07.026.
- [39] S. Sarkar, J. A. Hoffmann, and J. Park. “Micro-Macroscopic Modeling of a Lithium-Ion Battery by Considering Grain Boundaries of Active Materials”. In: *Electrochimica Acta* 393 (Oct. 2021), p. 139052. DOI: 10.1016/j.electacta.2021.139052.
- [40] X.-L. Peng and B.-X. Xu. “Unraveling Impacts of Polycrystalline Microstructures on Ionic Conductivity of Ceramic Electrolytes by Computational Homogenization and Machine Learning”. In: *J. Appl. Phys.* 136.10 (Sept. 2024), p. 105101. DOI: 10.1063/5.0223138.
- [41] Y. Bai, K. Zhao, Y. Liu, P. Stein, and B.-X. Xu. “A Chemo-Mechanical Grain Boundary Model and Its Application to Understand the Damage of Li-ion Battery Materials”. In: *Scripta Mater.* 183 (July 2020), pp. 45–49. DOI: 10.1016/j.scriptamat.2020.03.027.
- [42] P. W. Hoffrogge, A. Mukherjee, E. S. Nani, P. G. K. Amos, F. Wang, D. Schneider, and B. Nestler. “Multiphase-Field Model for Surface Diffusion and Attachment Kinetics in the Grand-Potential Framework”. In: *Phys. Rev. E* 103.3 (Mar. 2021), p. 033307. DOI: 10.1103/PhysRevE.103.033307.
- [43] S. Daubner, M. Weichel, P. W. Hoffrogge, D. Schneider, and B. Nestler. “Modeling Anisotropic Transport in Polycrystalline Battery Materials”. In: *Batteries* 9.6 (June 2023), p. 310. DOI: 10.3390/batteries9060310.
- [44] P. E. L’vov, R. T. Sibatov, and V. V. Svetukhin. “Anisotropic Grain Boundary Diffusion in Binary Alloys: Phase-field Approach”. In: *Mater. Today Commun.* 35 (June 2023), p. 106209. DOI: 10.1016/j.mtcomm.2023.106209.
- [45] L. H. J. Raijmakers, D. L. Danilov, R. -. Eichel, and P. H. L. Notten. “An Advanced All-Solid-State Li-ion Battery Model”. In: *Electrochim. Acta* 330 (Jan. 2020), p. 135147. DOI: 10.1016/j.electacta.2019.135147.
- [46] M. Ostoja-Starzewski and S. I. Ranganathan. “Scaling and Homogenization in Spatially Random Composites”. In: *Math. Methods Models Compos.* Vol. Volume 5. Computational and Experimental Methods in Structures. IMPERIAL COLLEGE PRESS, Nov. 2011, pp. 61–101. DOI: 10.1142/9781848167858_0002.
- [47] S. Arrhenius. “Über die Dissociationswärme und den Einfluss der Temperatur auf den Dissoziationsgrad der Elektrolyte”. In: *Z. Phys. Chem.* 4U.1 (July 1889), pp. 96–116. DOI: 10.1515/zpch-1889-0408.
- [48] T. Mori and T. Mura. “Blocking Effect of Inclusions on Grain Boundary Sliding; Spherical Grain Approximation”. In: *J. Mech. Phys. Solids* 35.5 (Jan. 1987), pp. 631–641. DOI: 10.1016/0022-5096(87)90020-2.

- [49] M. Pezzotta, Z. L. Zhang, M. Jensen, T. Grande, and M. -. Einarsrud. “Cohesive Zone Modeling of Grain Boundary Microcracking Induced by Thermal Anisotropy in Titanium Diboride Ceramics”. In: *Comput. Mater. Sci.* 43.3 (Sept. 2008), pp. 440–449. DOI: 10.1016/j.commatsci.2007.12.011.
- [50] S. Wulfinghoff. “A Generalized Cohesive Zone Model and a Grain Boundary Yield Criterion for Gradient Plasticity Derived from Surface- and Interface-Related Arguments”. In: *Int. J. Plast.* 92 (May 2017), pp. 57–78. DOI: 10.1016/j.ijplas.2017.02.006.
- [51] A. Needleman. “An Analysis of Decohesion along an Imperfect Interface”. In: *Int. J. Fract.* 42.1 (Jan. 1990), pp. 21–40. DOI: 10.1007/BF00018611.
- [52] M. J. van den Bosch, P. J. G. Schreurs, and M. G. D. Geers. “An Improved Description of the Exponential Xu and Needleman Cohesive Zone Law for Mixed-Mode Decohesion”. In: *Eng. Fract. Mech.* 73.9 (June 2006), pp. 1220–1234. DOI: 10.1016/j.engfracmech.2005.12.006.
- [53] M. Leuschner, F. Fritzen, J. A. W. van Dommelen, and J. P. M. Hoefnagels. “Potential-Based Constitutive Models for Cohesive Interfaces: Theory, Implementation and Examples”. In: *Compos. Part B: Eng.* 68 (Jan. 2015), pp. 38–50. DOI: 10.1016/j.compositesb.2014.08.024.
- [54] F. Aurenhammer. “Voronoi Diagrams—a Survey of a Fundamental Geometric Data Structure”. In: *ACM Comput. Surv.* 23.3 (Sept. 1991), pp. 345–405. DOI: 10.1145/116873.116880.
- [55] F. Fritzen, T. Böhlke, and E. Schnack. “Periodic Three-Dimensional Mesh Generation for Crystalline Aggregates Based on Voronoi Tessellations”. In: *Comput. Mech.* 43.5 (Apr. 2009), pp. 701–713. DOI: 10.1007/s00466-008-0339-2.
- [56] R. Quey, P. R. Dawson, and F. Barbe. “Large-Scale 3D Random Polycrystals for the Finite Element Method: Generation, Meshing and Remeshing”. In: *Comput. Methods Appl. Mech. Eng.* 200.17 (Apr. 2011), pp. 1729–1745. DOI: 10.1016/j.cma.2011.01.002.
- [57] M. V. Reddy, C. M. Julien, A. Mauger, and K. Zaghbi. “Sulfide and Oxide Inorganic Solid Electrolytes for All-Solid-State Li Batteries: A Review”. In: *Nanomaterials* 10.8 (Aug. 2020), p. 1606. DOI: 10.3390/nano10081606.
- [58] S. Keshav, J. Herb, and F. Fritzen. “Spectral Normalization and Voigt-Reuss Net: A Universal Approach to Microstructure-Property Forecasting with Physical Guarantees”. Apr. 2025. DOI: 10.48550/arXiv.2504.00712. arXiv: 2504.00712 [cs].
- [59] E. Buckingham. “On Physically Similar Systems; Illustrations of the Use of Dimensional Equations”. In: *Phys. Rev.* 4.4 (Oct. 1914), pp. 345–376. DOI: 10.1103/PhysRev.4.345.
- [60] R. Quey and M. Kasemer. “The Neper/FEPX Project: Free / Open-source Polycrystal Generation, Deformation Simulation, and Post-processing”. In: *IOP Conf. Ser. Mater. Sci. Eng.* 1249.1 (July 2022), p. 012021. DOI: 10.1088/1757-899X/1249/1/012021.
- [61] V. P. Nguyen. “An Open Source Program to Generate Zero-Thickness Cohesive Interface Elements”. In: *Adv. Eng. Softw.* 74 (Aug. 2014), pp. 27–39. DOI: 10.1016/j.advengsoft.2014.04.002.
- [62] R. Hill. “The Elastic Behaviour of a Crystalline Aggregate”. In: *Proc. Phys. Soc. A* 65.5 (May 1952), pp. 349–354. DOI: 10.1088/0370-1298/65/5/307.
- [63] F. Fritzen and T. Böhlke. “Nonuniform Transformation Field Analysis of Materials with Morphological Anisotropy”. In: *Compos. Sci. Technol.* 71.4 (Feb. 2011), pp. 433–442. DOI: 10.1016/j.compscitech.2010.12.013.
- [64] A. Kumar, H. Barda, L. Klinger, M. W. Finnis, V. Lordi, E. Rabkin, and D. J. Srolovitz. “Anomalous Diffusion along Metal/Ceramic Interfaces”. In: *Nat. Commun.* 9.1 (Dec. 2018), p. 5251. DOI: 10.1038/s41467-018-07724-7.